Am J Cancer Res 2026;16(10):4579-4602
www.ajcr.us /ISSN:2156-6976/ajcr0174273

Original Article

Pharmacodynamic effects and mechanisms underlying hupehenine against hepatocellular carcinoma: in vitro and in vivo studies

Xi-Chun Huang[1*], Ying-Hua Luo[2*], Nan Wu[1,3,4], Quan Quan[1], Jun-Hao Li[1], Tian-Zhu Li[5], Cheng-Hao Jin[1,3,4]

[1]Department of Biochemistry and Molecular Biology, College of Life Science and Biotechnology, Heilongjiang Bayi Agricultural University, No. 5 Xinfeng Road, Daqing 163319, Heilongjiang, China; [2]Department of Grass Science, College of Animal Science and Veterinary Medicine, Heilongjiang Bayi Agricultural University, No. 5 Xinfeng Road, Daqing 163319, Heilongjiang, China; [3]Department of Food Science and Engineering, College of Food Science, Heilongjiang Bayi Agricultural University, No. 5 Xinfeng Road, Daqing 163319, Heilongjiang, China; [4]National Coarse Cereals Engineering Research Center, No. 26 Xinfa Street, Daqing 163319, Heilongjiang, China; [5]Department of Molecular Biology, College of Basic Medical Science, Chifeng University, No. 60 Tiedanan Street, Hongshan District, Chifeng 024000, Inner Mongolia Autonomous Region, China. [*]Equal contributors.

Received May 25, 2026; Accepted October 12, 2026; Epub October 15, 2026; Published October 30, 2026

Abstract: Hupehenine (HUP) is an alkaloid isolated from *Fritillaria hupehensis.* However, its role in cancer and the associated molecular pathways are unclear. The purpose of this study was to investigate the inhibitory effects of HUP on hepatocellular carcinoma (HCC) and the molecular mechanisms underlying these effects. Experiments were conducted using HCC cell lines, BALB/c mouse HepG2 xenograft models, and bioinformatics analyses. HUP exerted a pronounced effect on 12 traditional cell lines that represent the four most deadly types of cancer, with HCC cells showing a particularly strong killing effect. Nonetheless, healthy cells showed no apparent toxicity. Furthermore, HUP induced cell death, suppressed cell cycle progression, and inhibited cell migration in association with reduced epidermal growth factor receptor (EGFR) phosphorylation, intracellular reactive oxygen species (ROS) accumulation, and phosphoinositide 3-kinase (PI3K)-protein kinase B (AKT) signaling suppression. The relevance of these signaling processes in HUP's effects was further supported by pharmacological interventions based on an EGFR agonist and inhibitor, a ROS scavenger, and an AKT inhibitor. In vivo experiments demonstrated that HUP inhibited xenograft growth in a dose-responsive manner and prevented tumor progression in mouse models. The underlying molecular mechanism of HUP was further confirmed by immunohistochemical analysis, which demonstrated that HUP markedly reduced the levels of critical signaling molecules, including p-EGFR, p-PI3K, and p-AKT. Importantly, HUP did not damage major organs, suggesting short-term tolerability under the tested conditions. In summary, HUP exerts anti-HCC effects associated with EGFR signaling suppression, ROS accumulation, and inhibition of the PI3K-AKT pathway, providing experimental evidence for its pharmacological mechanism and supporting further preclinical investigation.

Keywords: Hupehenine, natural alkaloid, hepatocellular carcinoma, epidermal growth factor receptor, reactive oxygen species

Introduction

According to the Global Cancer Epidemiology Report, lung, colorectal, liver, and breast cancers are the four primary causes of cancer-related mortality [1]. Among these, hepatocellular carcinoma (HCC) poses a major hazard to human health owing to its insidious onset, rapid progression, and dismal prognosis [2]. Despite the continuous advancements in surgery, chemotherapy, targeted therapy, and immunotherapy, their efficacy is severely limited by drug resistance, toxic adverse effects, and high rates of postoperative recurrence. Therefore, identifying safe and efficient anti-HCC drugs from natural small-molecule compounds and clarifying their molecular mechanisms is warranted.

Natural compounds derived from Chinese medicinal herbs have the benefits of a diverse range of pharmacological activities and low tox-

https://doi.org/10.62347/VXXI4571

icity [3-5]. *Fritillaria hupehensis* has been used in Traditional Chinese Medicine for over 2,000 years, primarily because its bulbs are rich in active alkaloid compounds that help relieve coughs and remove mucus [6]. *Fritillaria hupehensis* bulbs are the source of hupehenine (HUP), a natural active alkaloid component [7, 8]. However, its anticancer activity has not yet been systematically investigated, and the underlying mechanisms remain unclear.

The human body uses apoptosis clearance to eliminate malignant tumor cells, which is essential for maintaining tissue homeostasis [9-13]. This reaction is regulated by many signaling molecules, such as Bcl-2 family proteins, caspase-3, and PARP [14-16]. Reactive oxygen species (ROS) spike in response to external stimuli, causing oxidative damage that activates downstream apoptotic pathways and induces tumor cell death [17]. The aberrant activation of signaling pathways by ROS is pivotal in the onset and development of HCC [18, 19], establishing it as a key research area for targeted therapeutic approaches to HCC [20].

Metastasis enables cancer cells to disseminate to remote organs, leading to most cancer-related fatalities [21-23]. Epithelial-mesenchymal transition (EMT) may influence various physiological processes and may be regulated by the glycogen synthase kinase 3 beta (GSK-3β)/β-catenin/Snail family transcriptional repressor 1 (SNAI1) axis [24, 25]. Upon GSK-3β activity inhibition, β-catenin accumulates and translocates to the nucleus, triggering the downstream transcription of SNAI1. This promotes the migration of tumor cells by downregulating the epithelial marker E-cadherin and upregulating the mesenchymal marker N-cadherin [26]. The epidermal growth factor receptor (EGFR)-phosphoinositide 3-kinase (PI3K)-protein kinase B (AKT) pathway is a crucial upstream regulatory node that can positively activate this axis, further promoting EMT activation and tumor metastasis [27, 28].

This research aimed to investigate the impact of HUP on cell viability across 12 cell lines representing four cancer types and established cell models for subsequent experiments. The potential HUP targets and pathways in HCC were predicted through a bioinformatics analysis. Potential interactions between HUP and candidate proteins were further explored using molecular docking. This study examined the regulatory implications of HUP on apoptosis, cell cycle arrest, and migration within HCC cells, along with the underlying mechanisms. The antitumor effects and safety profile of HUP were assessed in vivo using a nude mouse xenograft model, providing experimental evidence to support further preclinical investigation of HUP.

Materials and methods

Drugs and reagents

HUP and 5-fluorouracil (5-FU) were purchased from Sigma-Aldrich (St. Louis, MO, USA). Two compounds were solubilized in dimethyl sulfoxide (DMSO, Solarbio, Beijing, China) to prepare a stock solution (20 mM). At the maximum HUP concentration of 80 μM used in the concentration-response assay, the final DMSO concentration was 0.4% (v/v), and it remained below 0.1% (v/v) in all subsequent mechanistic experiments. N-acetylcysteine (NAC), EGFR agonist NSC228155, and the EGFR tyrosine kinase inhibitor gefitinib were purchased from Solarbio. The AKT inhibitor (HY10249) was purchased from MedChemExpress (Princeton, USA). The remaining chemical reagents were all of analytical grade.

Cell lines and cell culture

This study used various human tumor and healthy cell lines. The lung cancer cell lines A549, NCI-H82, and NCI-H460, colon cancer cell lines HCT116, SW480, and HT-29, liver cancer cell lines Huh-7, HepG2, and Hep3B, breast cancer cell lines MDA-MB-231, MCF-7, and T47D, and the human normal embryonic lung fibroblast cell line IMR-90 were all purchased from the American Type Culture Collection (ATCC, Virginia, USA). The human embryonic kidney cell line 293T was purchased from Sage Biotechnology (Shanghai, China), and the human healthy liver cell line MIHA was obtained from Otwo Biotech (Shenzhen, China). Each cell line was exposed to a high-glucose medium enriched with 10% fetal bovine serum (FBS) and 1% penicillin-streptomycin (Gibco, MA, USA).

Cell viability and cytotoxicity

The impact of HUP on cell viability was assessed by the Cell Counting Kit-8 (CCK-8) assay. A549,

NCI-H82, NCI-H460, HCT116, SW480, HT-29, Huh-7, HepG2, Hep3B, MDA-MB-231, MCF-7, T47D, MIHA, IMR-90, and 293T cells were seeded in 96-well plates at a density of 1×10^4 cells/well. After 24 h of cultivation, these cells were treated with HUP or 5-FU at concentrations of 2.5, 5, 10, 20, 40, and 80 μM for 6, 12, 18, 24, and 30 h. 5-FU served as a positive control for comparing antitumor efficacy. After incubation with the CCK-8 reagent, the optical density was measured at 450 nm using a microplate reader (Tecan, Maennedorf, Switzerland). HepG2 cells were cultivated for 24 h at a density of 1×10^5 cells/well in six-well plates. These cells were exposed to HUP (10.38 μM) or 5-FU for 6, 12, and 24 h. The pellets were combined with an equivalent volume of 0.4% trypan blue solution and stained for 3 min. Finally, the stained cells were visualized under an inverted microscope (Mingmei Optoelectronics, Guangzhou, China).

Hoechst/PI double staining

To determine whether HUP had a cytotoxic effect on HepG2 cells, apoptotic morphology was detected by Hoechst/PI double staining. HepG2 cells were cultured in six-well plates for 24 h and treated with HUP (10.38 μM) or 5-FU for 6, 12, and 24 h. After staining with Hoechst 33342 and propidium iodide (PI) solution (Solarbio) for 15 min, a fluorescence microscope (EVOS FL, Thermo Fisher Scientific, MA, USA) was used to analyze changes in cell morphology.

Bioinformatics

The bioinformatics analysis aimed to predict the potential targets and associated pathways of HUP. The 2D and 3D structures of HUP were downloaded from the PubChem database (https://pubchem.ncbi.nlm.nih.gov). Then, the Swiss Target Prediction platform (http://swisstargetprediction.ch) was used to identify the drug targets. HCC-related targets were sourced from the GeneCards database (https://www.genecards.org/). The common targets of drugs and diseases were analyzed using the STRING database (https://string-db.org), and the protein-protein interaction (PPI) network was visualized using Cytoscape 3.8.2. The functional annotation analyses of Gene Ontology (GO) and the enrichment of Kyoto Encyclopedia of Genes and Genomes (KEGG) pathways for the shared targets were conducted using the DAVID database (https://david.ncifcrf.gov/).

Molecular docking

Molecular docking was conducted to predict potential binding interactions between HUP and candidate proteins. Structures of key target proteins were downloaded from the RCSB PDB database (https://www.rcsb.org/). The ligands and proteins underwent pre-treatment using AutoDockTools-1.5.6. Docking was conducted using AutoDock 4.2; Supplementary Table 1 contains the target-specific grid parameters. Each target underwent 10 independent docking runs, and the lowest-energy conformation was selected for analysis and PyMOL visualization.

Apoptosis

The apoptotic rate of HUP-treated HepG2 cells was assessed using Annexin V-FITC/PI fluorescent double staining along with flow cytometry. HepG2 cells were cultured in six-well plates for 24 h and treated with HUP (10.38 μM) or 5-FU for 6, 12, and 24 h. They were harvested and subjected to staining with Annexin V-FITC and PI solutions (Solarbio) for 20 min in a dark environment. Fluorescence microscopy was used to observe the stained cells, and a flow cytometer (Sysmex, Kobe, Japan) was used to measure the percentage of apoptotic cells.

Mitochondrial membrane potential

In HUP-treated HepG2 cells, the mitochondrial membrane potential was assessed using JC-1 staining. HepG2 cells were cultured in six-well plates for 24 h and treated with HUP (10.38 μM) or 5-FU for 6, 12, and 24 h. They were collected and treated with 500 μL of JC-1 staining solution (Solarbio) for 30 min. After centrifugation, the supernatant was discarded, and the cells were resuspended in 500 μL of JC-1 buffer, followed by another round of centrifugation. Finally, the fluorescence intensity was measured using flow cytometry.

Intracellular ROS levels

The 2',7'-dichlorodihydrofluorescein diacetate (DCFH-DA) fluorescent probe was used to detect intracellular ROS levels in HUP-treated HepG2 cells. HepG2 cells were cultured in six-

well plates for 24 h and treated with HUP (10.38 μM) or 5-FU for 6, 12, and 24 h. After collecting the cells, they were treated with 10 μM DCFH-DA (Solarbio) in a 37°C water bath for 30 min in the dark. Fluorescence microscopy was used to observe changes in ROS levels, and flow cytometry was used to quantify them. In the scavenger experiment, cells were pre-treated with 10 mM NAC for 1 h, followed by co-treatment with HUP for 24 h. Next, they were analyzed for ROS levels. The NAC concentration was selected based on an initial cytotoxicity assessment, which showed no significant effect on HepG2 cell viability (data not shown). In the EGFR inhibitor experiment, cells were pretreated with 10 μM gefitinib for 1 h, followed by co-treatment with HUP for 24 h. Finally, intracellular ROS levels were measured by flow cytometry. For the concentration-response experiment, HepG2 cells were treated with HUP at 2.5, 5, or 10 μM for 6 h, followed by DCFH-DA-based flow cytometric analysis.

Cell cycle distribution

HUP-treated HepG2 cells were analyzed for the Ki67-positive cell percentage and cell cycle distribution using Ki67 and PI staining. After culturing for 12 h, HepG2 cells were treated with HUP (10.38 μM) or 5-FU for 6, 12, and 24 h. After fixation and permeabilization, the cells were treated with a Ki67 antibody (Solarbio), and the proportion of Ki67-positive cells was assessed using a fluorescence microscope. After fixing the cells with 70% ethanol overnight, they were incubated with 100 μL of RNase A (10 μg/mL) and 400 μL of PI staining solution (10 μg/mL) for 30 min. The DNA content was measured using flow cytometry.

Transwell migration and wound healing

Transwell and wound healing assays were used to assess the impact of HUP on the migratory capacity of HepG2 cells. These cells were seeded in six-well plates at 1×10^5 cells/well. In the wound healing assay, a sterile 200 μL pipette tip was used to create scratches. Transwell migration (1% FBS upper/10% FBS lower) was conducted using HUP (10.38 μM) or 5-FU for 6, 12, and 24 h. Cells that shifted to the underside were stained with 1% crystal violet and photographed using an inverted microscope.

Western blotting

Western blotting was used to measure the protein expression in HUP-treated HepG2 cells. HepG2 cells were seeded in six-well plates at 1×10^5 cells/well and cultured for 24 h. For the concentration-response experiment, HepG2 cells were treated with HUP at 2.5, 5, or 10 μM for 6 h, and p-EGFR, EGFR, p-AKT, and AKT levels were examined by western blotting. For the EGFR agonist and AKT inhibitor experiments, cells were pretreated with either NSC228155 (10 μM) or HY10249 (10 μM) for 2 h. Then, they were co-treated with HUP for 24 h. To obtain the supernatant, after lysis, the cells were centrifuged at 12,000 rpm for 30 min. The protein concentration was determined, and 40 μg of the total protein in each lane was separated by 8% to 12% SDS-PAGE and transferred onto 0.45 μm PVDF membranes. The membranes were incubated with primary antibodies at 4°C overnight, followed by corresponding secondary antibodies. Quantitative analysis was conducted using Image J software.

The following antibodies were used: the internal reference β-actin, apoptosis-related proteins (Bad, Bcl-2, Bax, Cyto C, cleaved-caspase-3, pro-caspase-3, pro-PARP, and cleaved-PARP), EGFR-PI3K-AKT pathway proteins (EGFR, p-EGFR, p-PI3K, PI3K, p-AKT, and AKT), nuclear factor kappa B (NF-κB) pathway proteins (NF-κB, inhibitor of nuclear factor kappa B (I-κB)), Oxidative stress-related proteins (Nrf2, HO-1, SOD, CAT, and Gpx1), Cell cycle-related proteins (CDK2, CDK4, CDK6, cyclin D, cyclin E, p21, and p27), and EMT-related proteins (p-GSK3β, GSK3β, β-catenin, SNAI1, E-cadherin, and N-cadherin). Supplementary Table 2 contains the sources and catalog numbers of all primary antibodies.

BALB/c nude mouse model and experimental design

Five-week-old male BALB/c nude mice were acquired from Liaoning Changsheng Biotechnology Co., Ltd. and housed under specific pathogen-free conditions to allow for a week of acclimatization before the experiment. The mice were injected into the lateral ribs with 100 μL of HepG2 cell suspension (2×10^6 cells/100 μL). Mice that failed to develop tumors within 7 days of inoculation were exclud-

ed from subsequent grouping. No unexpected deaths occurred during treatment. Ten nude mice per group were randomly divided into healthy untreated, vehicle control (0.1% DMSO in normal saline), 5-FU (10 mg/kg), HUP (1 mg/kg), HUP (10 mg/kg), and HUP (50 mg/kg) treatment groups. The vehicle control group received an equal volume of 0.1% DMSO in normal saline. The mentioned drugs were administered intraperitoneally every 2 days for 16 days. At the end of treatment, mice were humanely killed by cervical dislocation. Tumor volume was calculated as given below: Tumor volume = (short diameter^2 × long diameter)/2. Organ index (%) = [organ weight (g)/live body weight (g)] × 100%.

All animal experiments were approved by the Science and Technology Ethics Committee of Heilongjiang Bayi Agricultural University (SMKXJSXY2025045).

Hematoxylin and eosin staining

Hematoxylin and eosin (H&E) staining was used to analyze pathological changes in tumor tissues in the healthy, solvent control, and treatment groups. The sections underwent H&E staining (xylene 2 × 10 min, 100% ethanol 2 × 1 min, 80%/75%/50% ethanol 1 min each, H_2O 3 min; hematoxylin 5 min, 1% HCl-EtOH 2 s, H_2O 3 min, 0.8% ammonia 1 s, H_2O 5 min; and eosin 1 min, 95% ethanol 2 × 1 min, 100% ethanol 2 × 1 min, xylene 2 × 1 min). The slides were mounted with neutral resin and observed under a light microscope. All reagents for H&E staining were purchased from Solarbio.

Immunohistochemistry

Correlated protein expression in tumor tissues was detected using immunohistochemistry. Briefly, 5-μm-thick tissue sections were deparaffinized and rehydrated (xylene 2 × 10 min, 100% ethanol 2 × 1 min, 80%/75%/50% ethanol 1 min each, H_2O 3 min). Antigen retrieval was conducted in 10 mM sodium citrate buffer (pH 6.0) through microwave heating at 95°C for 20 min. Subsequently, endogenous peroxidase was neutralized with H_2O_2 for 15 min, and blocking was conducted with FBS for 20 min. After incubation with both primary and secondary antibodies, the staining results were visualized using the 3,3'-diaminobenzidine (DAB) staining method. After counterstaining with hematoxylin, the sections were dehydrated, mounted, and examined under a light microscope. The primary antibodies used were p-EGFR (BOSTER, P00023-7, 1:50), p-PI3K (BOSTER, P00318-1, 1:50), p-AKT (Santa Cruz Biotechnology, sc-7985-R, 1:50), cleaved caspase-3 (Santa Cruz Biotechnology, sc-271028, 1:50), and cleaved PARP (BOSTER, M00122-2, 1:50). Other reagents used for immunohistochemistry were obtained from Solarbio.

Statistical analysis

Data were assessed for normality using the Shapiro-Wilk test and for homogeneity of variances using Levene's test. All data met these assumptions; therefore, one-way or two-way ANOVA followed by Tukey's or Dunnett's multiple comparisons test, as appropriate, was performed. Two-way repeated-measures ANOVA with Greenhouse-Geisser correction was used to evaluate the longitudinal tumor volume and body weight data. Half-maximal inhibitory concentration (IC_{50}) values were calculated by nonlinear regression using a log(inhibitor) versus normalized response (variable slope) model in GraphPad Prism 11.0. In vitro data are presented as the mean ± SD, whereas the in vivo tumor volume and organ index data are presented as the mean ± SEM. *P* values indicate the statistical significance of the indicated pairwise comparisons. Different letters indicate significant differences between groups ($P < 0.05$).

Results

HUP inhibited the viability of HCC cells

HUP exhibited strong cytotoxic effects against 12 cell lines from lung, colorectal, liver, and breast cancers. According to a comparison of the IC_{50} values, the killing effect was particularly significant against HCC (**Figure 1A**). HUP decreased the viability of three HCC cell lines in a concentration-dependent manner (2.5-80 μM), with effects comparable to those observed with the positive control 5-FU (**Figure 1B** and **1C**). Additionally, HUP did not exert any noticeable negative effects on the three healthy cell lines (**Figure 1D** and **1E**). **Figure 1A** and **1B** display the concentration-response data for IC_{50} calculation. HepG2 cells were chosen for further research because they exhibited the lowest IC_{50} value (10.38 μM) of all the HCC cell lines.

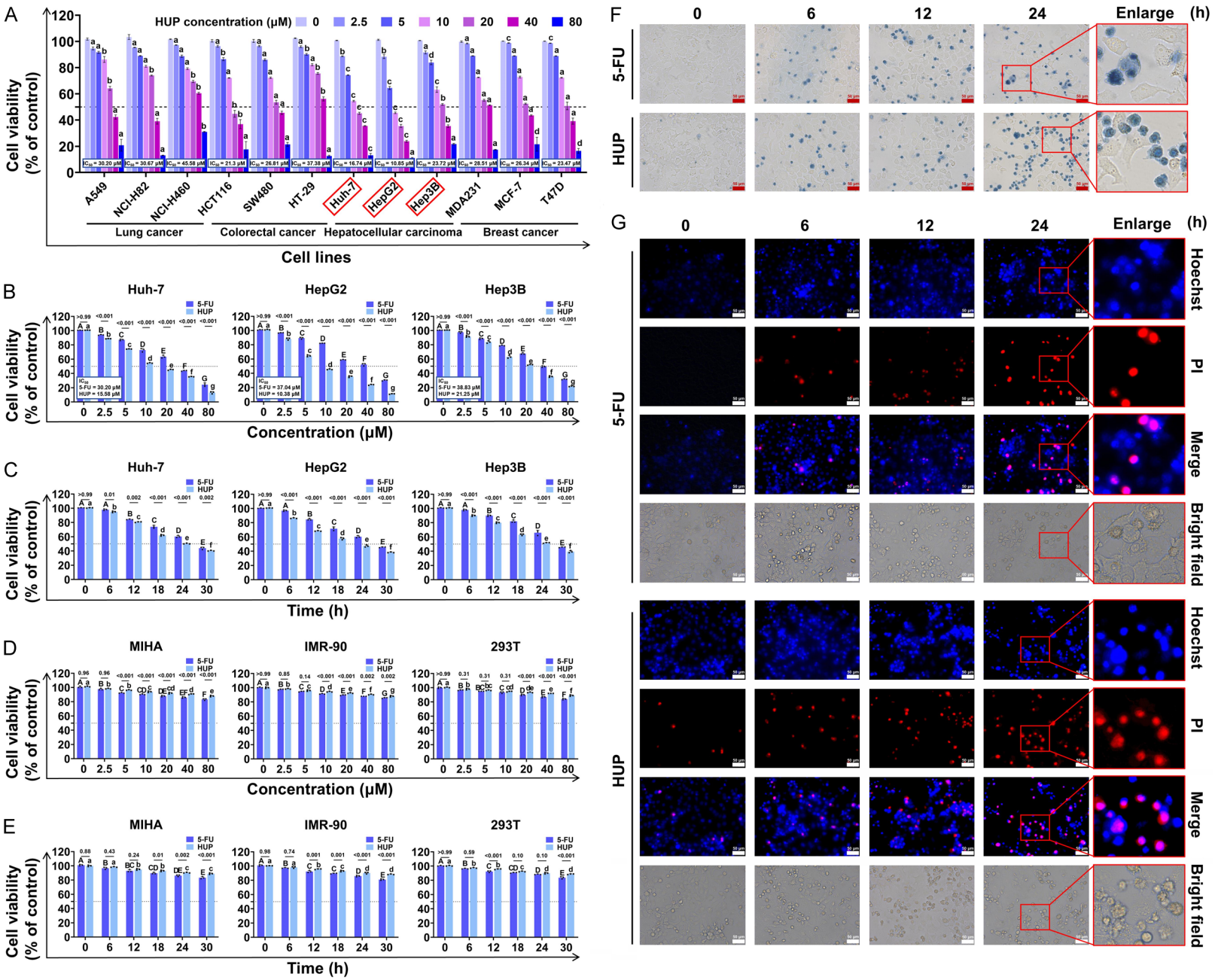

A
HUP concentration (μM) 0 2.5 5 10 20 40 80
Cell viability (% of control)
A549
NCI-H82
NCI-H460
HCT116
SW480
HT-29
Huh-7
HepG2
Hep3B
MDA231
MCF-7
T47D
Lung cancer
Colorectal cancer
Hepatocellular carcinoma
Breast cancer
Cell lines
B
Huh-7
HepG2
Hep3B
5-FU
HUP
Concentration (μM)
C
Time (h)
D
MIHA
IMR-90
293T
E
F
0
6
12
24
Enlarge
(h)
5-FU
HUP
G
Hoechst
PI
Merge
Bright field

Figure 1. Hupehenine (HUP) selectively inhibited hepatocellular carcinoma (HCC) cell proliferation. (A) Viability of lung cancer (A549, NCI-H82, NCI-H460), colorectal cancer (HCT116, SW480, HT-29), HCC (Huh-7, HepG2, Hep3B), and breast cancer (MDA-MB-231, MCF-7, T47D) cells after treatment with different concentrations (2.5, 5, 10, 20, 40, and 80 μM) of HUP for 24 h, as measured using the Cell Counting Kit-8 (CCK-8) assay. (B) Viability of three HCC cell types (HepG2, Huh-7, and Hep3B) after treatment with different concentrations (2.5, 5, 10, 20, 40, and 80 μM) of HUP and 5-fluorouracil (5-FU) for 24 h, as measured using the CCK-8 assay. (C) Viability of three types of HCC cells (HepG2, Huh-7, and Hep3B) after treatment with HUP and 5-FU for different durations (6, 12, 18, 24, and 30 h), as measured using the CCK-8 assay. (D) Viability of three types of normal cells (MIHA, IMR-90, and 293T) after treatment with different concentrations (2.5, 5, 10, 20, 40, and 80 μM) of HUP and 5-FU for 24 h, as measured using the CCK-8 assay. (E) Viability of three types of normal cells (MIHA, IMR-90, and 293T) after treatment with HUP and 5-FU for different durations (6, 12, 18, 24, and 30 h), as measured by the CCK-8 assay. (F) Trypan blue staining to observe morphological changes in HepG2 cells after treatment with HUP and 5-FU for different durations (6, 12, and 24 h). Scale bar: 50 μm. (G) Hoechst 33342/propidium iodide (PI) double staining to detect changes in the apoptotic morphology of HepG2 cells under a fluorescence microscope after treatment with HUP and 5-FU for different durations (6, 12, and 24 h). Scale bar: 50 μm. In (A), different lowercase letters indicate significant differences among HUP concentrations within each cell line. In (B-E), uppercase and lowercase letters indicate differences within the 5-FU and HUP groups, respectively; exact *p* values indicate comparisons between 5-FU and HUP at the same concentration or time point. n = 3. magnification: 400×.

Trypan blue staining further confirmed an increase in the number of dead cells after HUP treatment (**Figure 1F**). Hoechst 33342/PI double-staining assay showed a time-dependent increase in both blue and red fluorescence signals in HepG2 cells after HUP treatment, together with significant changes in nuclear morphology (**Figure 1G**). Trypan blue and Hoechst 33342/PI double staining were used to confirm the cytotoxic effect of HUP on HepG2 cells, demonstrating greater efficacy than the 5-FU control group. In summary, HUP selectively inhibited the viability of HCC cells without significantly affecting healthy cells. Furthermore, HepG2 cells may serve as an in vitro model in future studies.

HUP and HCC bioinformatics analysis and molecular docking

Figure 2A presents the 2D and 3D structural configurations of HUP. Overall, 34 overlapping targets were identified between HUP and HCC (**Figure 2B**). The STRING database was used to construct PPI networks for these core targets, and the networks were visualized using Cytoscape software. EGFR, AKT1, and Bcl-2 emerged as significant hub genes (**Figure 2C**). GO functional enrichment evaluation showed that these targets predominantly regulated biological processes related to apoptosis and protein phosphorylation, as well as those related to cellular components and molecular functions (**Figure 2D**). The KEGG pathway enrichment analysis indicated that the core targets were significantly enriched in the PI3K-AKT, NF-κB, ROS, and apoptosis pathways (**Figure 2E**). **Figure 2F** illustrates the distribution of core targets across the functional categories.

Molecular docking predicted favorable interactions between HUP and EGFR (-8.23 kcal/mol), AKT1 (-7.86 kcal/mol), and Bcl-2 (-8.87 kcal/mol). The predicted binding energies with SRC, TNF, and HSP90AA1 were -7.08, -7.22, and -6.61 kcal/mol, respectively (**Figure 2G**). These results suggest potential interactions between HUP and candidate proteins. Together with the bioinformatics analysis results, they support further investigation of the EGFR-PI3K-AKT and related pathways.

HUP induced mitochondrial apoptosis in HepG2 cells

Fluorescence microscopy showed that the fluorescence signals corresponding to green (Annexin V) and red (PI) exhibited a time-dependent increase after HUP treatment at 6, 12, and 24 h. These findings indicate early and late apoptotic/necrotic cells, exhibiting a pattern similar to that observed in the positive control 5-FU (**Figure 3A**). The apoptotic rate significantly increased in a time-dependent manner after HUP treatment, as confirmed by flow cytometry (**Figure 3B**). JC-1 staining was used to measure the decrease in mitochondrial membrane potential (ΔΨm). HUP treatment resulted in a progressive shift in JC-1 from its combined state, distinguished by red fluorescence, to its monomeric state, distinguished by green fluorescence. This shift indicates a decrease in the ΔΨm over time (**Figure 3C**).

According to Western blot analysis, HUP treatment upregulated the pro-apoptotic proteins Bad and Bax, downregulated the anti-apoptotic protein Bcl-2, promoted Cyto C release, and activated caspase-3 and PARP in a time-depen-

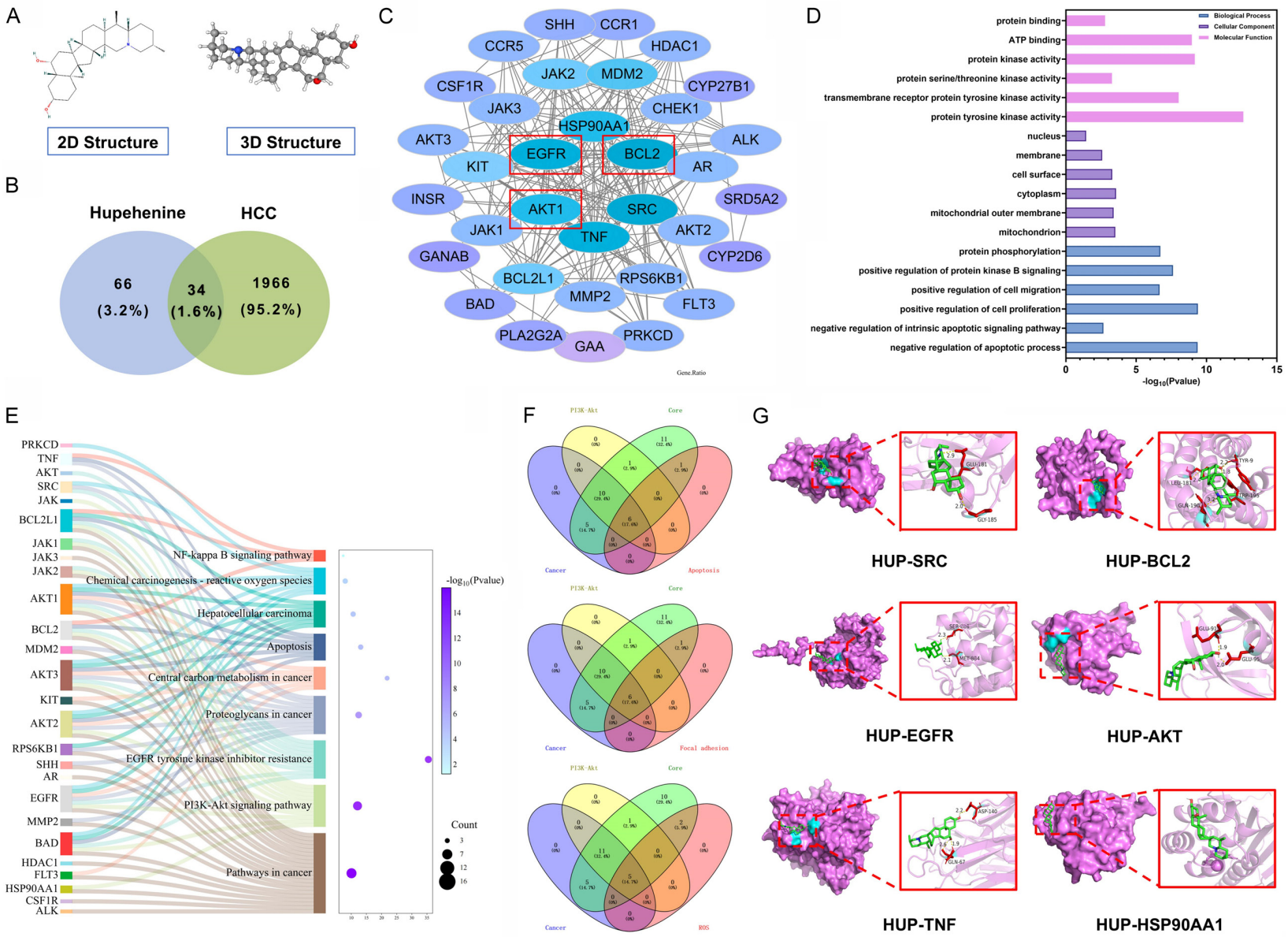
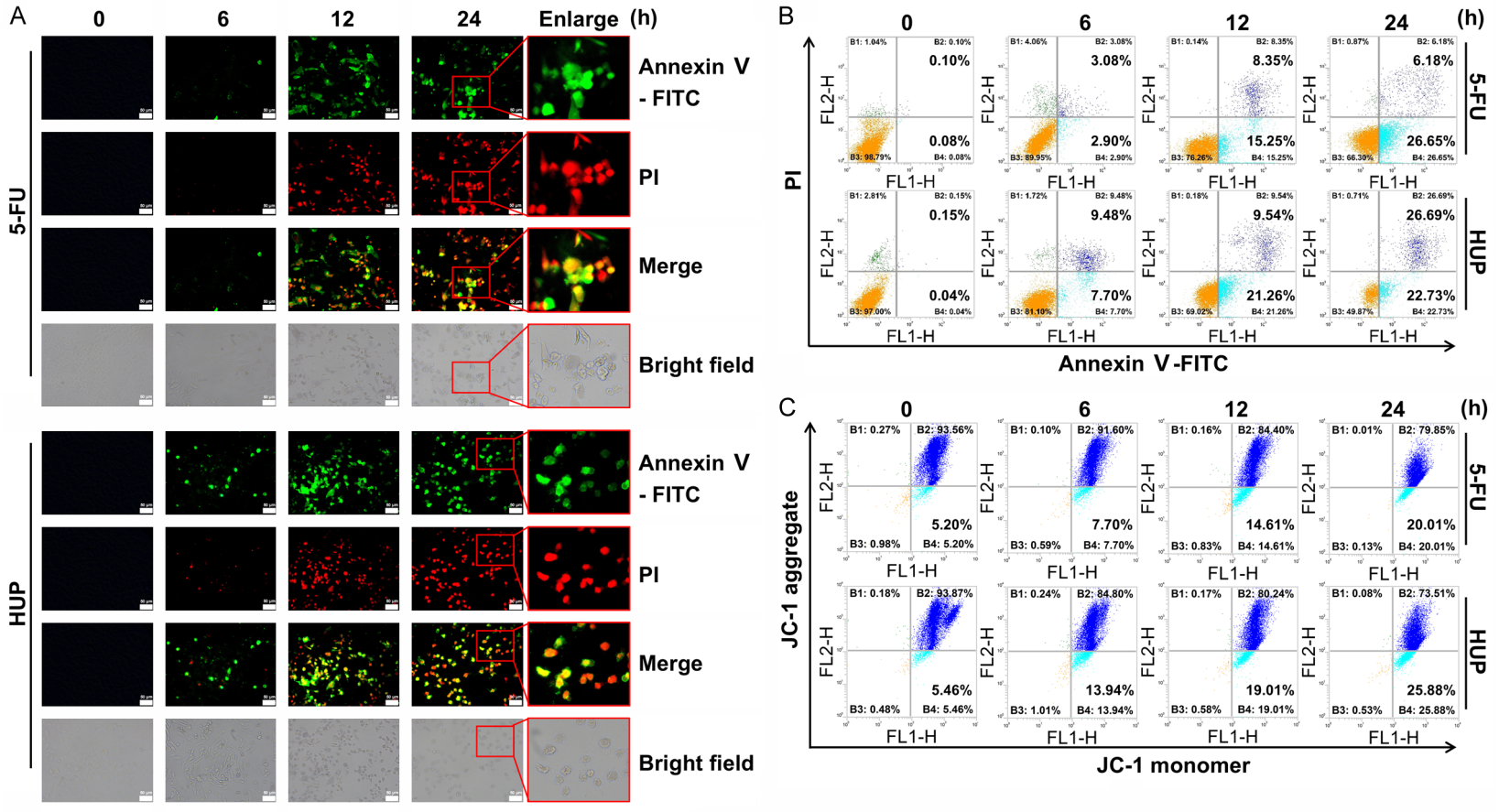

A
2D Structure
3D Structure
B
Hupehenine
HCC
66
(3.2%)
34
(1.6%)
1966
(95.2%)
C
SHH
CCR1
CCR5
HDAC1
JAK2
MDM2
CSF1R
CYP27B1
JAK3
CHEK1
HSP90AA1
AKT3
ALK
EGFR
BCL2
KIT
AR
INSR
SRD5A2
AKT1
SRC
JAK1
TNF
AKT2
GANAB
CYP2D6
BCL2L1
RPS6KB1
MMP2
BAD
FLT3
PLA2G2A
PRKCD
GAA
Gene.Ratio
D
Biological Process
Cellular Component
Molecular Function
protein binding
ATP binding
protein kinase activity
protein serine/threonine kinase activity
transmembrane receptor protein tyrosine kinase activity
protein tyrosine kinase activity
nucleus
membrane
cell surface
cytoplasm
mitochondrial outer membrane
mitochondrion
protein phosphorylation
positive regulation of protein kinase B signaling
positive regulation of cell migration
positive regulation of cell proliferation
negative regulation of intrinsic apoptotic signaling pathway
negative regulation of apoptotic process
0
5
10
15
-log10(Pvalue)
E
PRKCD
TNF
AKT
SRC
JAK
BCL2L1
JAK1
JAK3
JAK2
AKT1
BCL2
MDM2
AKT3
KIT
AKT2
RPS6KB1
SHH
AR
EGFR
MMP2
BAD
HDAC1
FLT3
HSP90AA1
CSF1R
ALK
NF-kappa B signaling pathway
Chemical carcinogenesis - reactive oxygen species
Hepatocellular carcinoma
Apoptosis
Central carbon metabolism in cancer
Proteoglycans in cancer
EGFR tyrosine kinase inhibitor resistance
PI3K-Akt signaling pathway
Pathways in cancer
-log10(Pvalue)
Count
F
PI3K-Akt
Core
Cancer
Apoptosis
Focal adhesion
ROS
G
HUP-SRC
HUP-BCL2
HUP-EGFR
HUP-AKT
HUP-TNF
HUP-HSP90AA1

Figure 2. Mechanism prediction results based on network pharmacology and molecular docking. A. 2D and 3D chemical structures of HUP. B. Analysis of the intersection targets between HUP and HCC disease targets identified 34 common targets. C. protein-protein interaction (PPI) network analysis of the 34 common targets, yielding the key hub genes. D. Gene Ontology (GO) enrichment analysis of the common targets, including biological process, cellular component, and molecular function categories. E. Kyoto Encyclopedia of Genes and Genomes (KEGG) pathway enrichment analysis of the common targets. F. Venn diagram of the distribution of core targets in different functional categories. G. Predicted molecular docking interactions of HUP with selected candidate proteins.



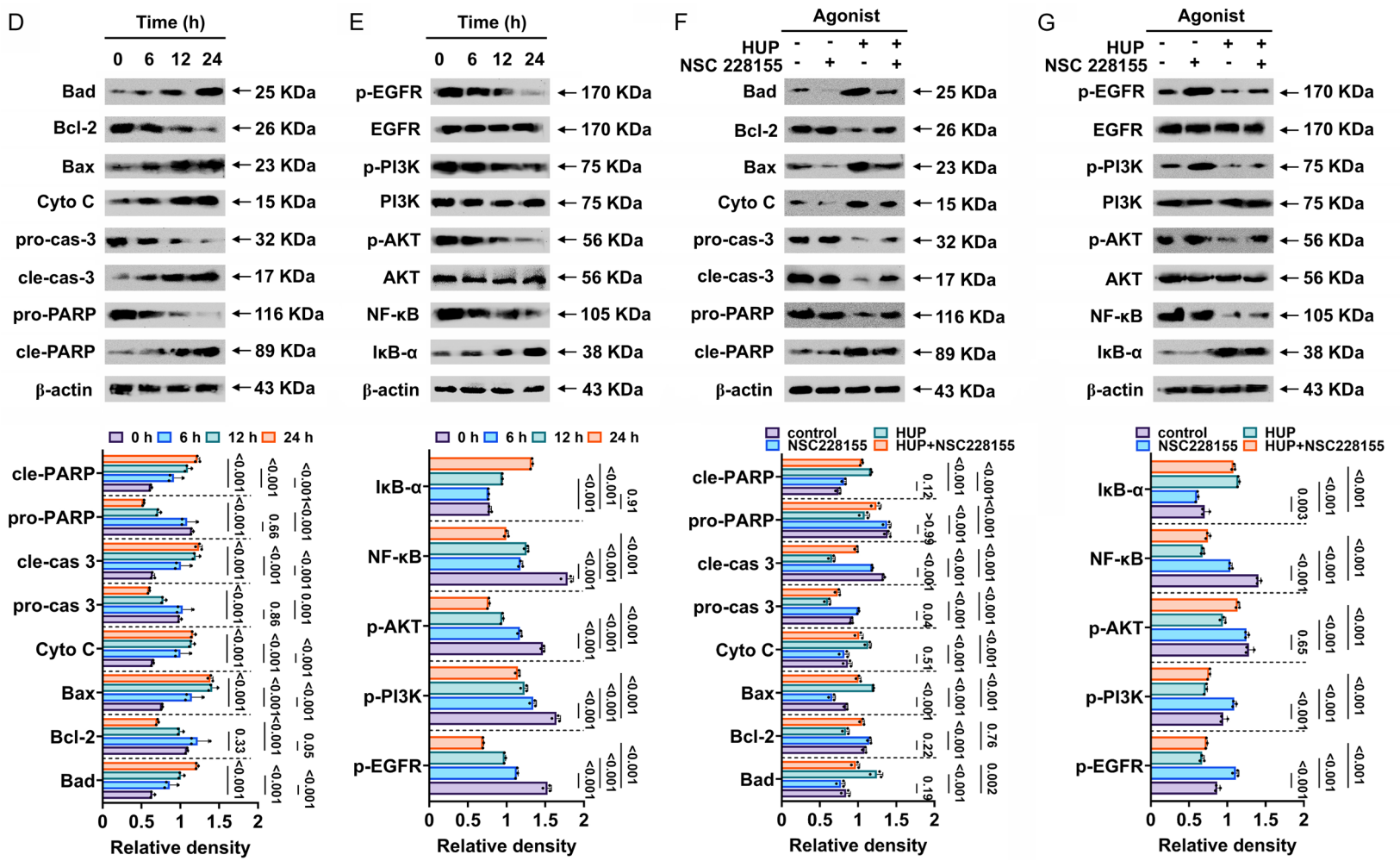


Figure 3. Mechanism of HUP-induced apoptosis in HepG2 cells. A. Annexin V-Fluorescein Isothiocyanate (FITC)/PI double-fluorescence staining was used to observe morphological changes in HepG2 cell apoptosis after treatment with HUP or 5-FU at different time points (6, 12, and 24 h). Scale bar: 50 μm. B. Flow cytometry combined with Annexin V-FITC/PI double fluorescence staining was used to quantitatively detect changes in the apoptosis rate of HepG2 cells after treatment with HUP or 5-FU at different time points (6, 12, and 24 h). C. Flow cytometry with JC-1 staining was used to detect changes in the mitochondrial membrane potential of HepG2 cells after treatment with HUP or 5-FU at different time points (6, 12, and 24 h). D. Expression levels of apoptosis-related proteins (Bad, Bcl-2, Bax, cytochrome c, pro-caspase-3, cleaved-caspase-3, pro-PARP, and cleaved-PARP) in HepG2 cells after treatment with HUP at different time points (6, 12, and 24 h) were measured by western blotting. E. Western blotting was used to detect changes in the expression levels of pathway-related proteins (p-epidermal growth factor receptor (EGFR), EGFR, p-phosphoinositide 3-kinase (PI3K), PI3K, p-protein kinase B (AKT), AKT, nuclear factor kappa B (NF-κB), and inhibitor of nuclear factor kappa B (I-κB)) in HepG2 cells after treatment with HUP at different time points (6, 12, and 24 h). F. Western blotting was performed to investigate the reversal effect of HUP on the expression of apoptosis-related proteins in HepG2 cells pre-treated with the EGFR agonist NSC228155. G. Western blot analysis was used to detect the reversal effect of HUP on the expression of EGFR-PI3K-AKT and NF-κB pathway-related proteins in HepG2 cells pre-treated with the EGFR agonist NSC228155. *P* value indicate the statistical significance of the indicated pairwise comparisons. n = 3. magnification: 400×.

dent manner (**Figure 3D**). Furthermore, HUP treatment decreased the phosphorylation levels of EGFR, PI3K, and AKT, without changing their total protein levels (**Figure 3E**). The EGFR agonist NSC228155 was used to determine whether this pathway facilitates HUP-induced apoptosis. Co-treatment with NSC228155 partially reversed HUP-induced alterations in apoptotic protein expression, and it reinstated the phosphorylation levels of EGFR, PI3K, and AKT (**Figure 3F** and **3G**). Collectively, HUP induces mitochondrial apoptosis in HepG2 cells in association with inhibition of the EGFR-PI3K-AKT pathway.

HUP-induced ROS accumulation contributes to PI3K-AKT regulation downstream of EGFR

HUP treatment resulted in a time-dependent rise in ROS production in HepG2 cells using fluorescence microscopy and flow cytometry (**Figure 4A** and **4C**). The ROS formation was successfully inhibited by NAC pre-treatment (**Figure 4B** and **4D**). Results of Annexin V-FITC/PI staining indicated that NAC substantially counteracted HUP-induced apoptosis (**Figure 4E**). DCFH-DA-based flow cytometry further showed that gefitinib increased intracellular ROS levels (**Figure 4F**).

Western blot analysis showed that HUP downregulated Nrf2 and its downstream antioxidant enzymes, HO-1, SOD, CAT, and Gpx1, suggesting suppression of the endogenous antioxidant defense system (**Figure 4G**). NAC pretreatment partially restored protein expression, suggesting a strong association between HUP-induced ROS accumulation and disruption of the Nrf2-related antioxidant defense system (**Figure 4H**). Consistently, NAC pre-treatment attenuated the HUP-mediated changes in apoptosis-related proteins, such as the upregulation of Bad and Bax, downregulation of Bcl-2, Cyto C release, and activation of caspase-3 and PARP (**Figure 4I**). Moreover, NAC pretreatment partially restored PI3K and AKT phosphorylation but did not reverse the HUP-induced decrease in EGFR phosphorylation (**Figure 4J**). The EGFR inhibitor gefitinib was used to further clarify the relationship between EGFR and ROS. Western blotting further showed that gefitinib reduced EGFR phosphorylation without affecting total EGFR expression (**Figure 4K**). These results corroborate the role of ROS in regulating PI3K/AKT signaling downstream of EGFR. To further examine the concentration-related effects of HUP at an early time point, HepG2 cells were treated with 2.5, 5, or 10 μM HUP for 6 h. HUP at 2.5 μM did not significantly reduce cell viability, whereas intracellular ROS signals increased and EGFR and AKT phosphorylation decreased across the concentration range. Notably, AKT phosphorylation was significantly reduced at 2.5 μM (Supplementary Figure 1).

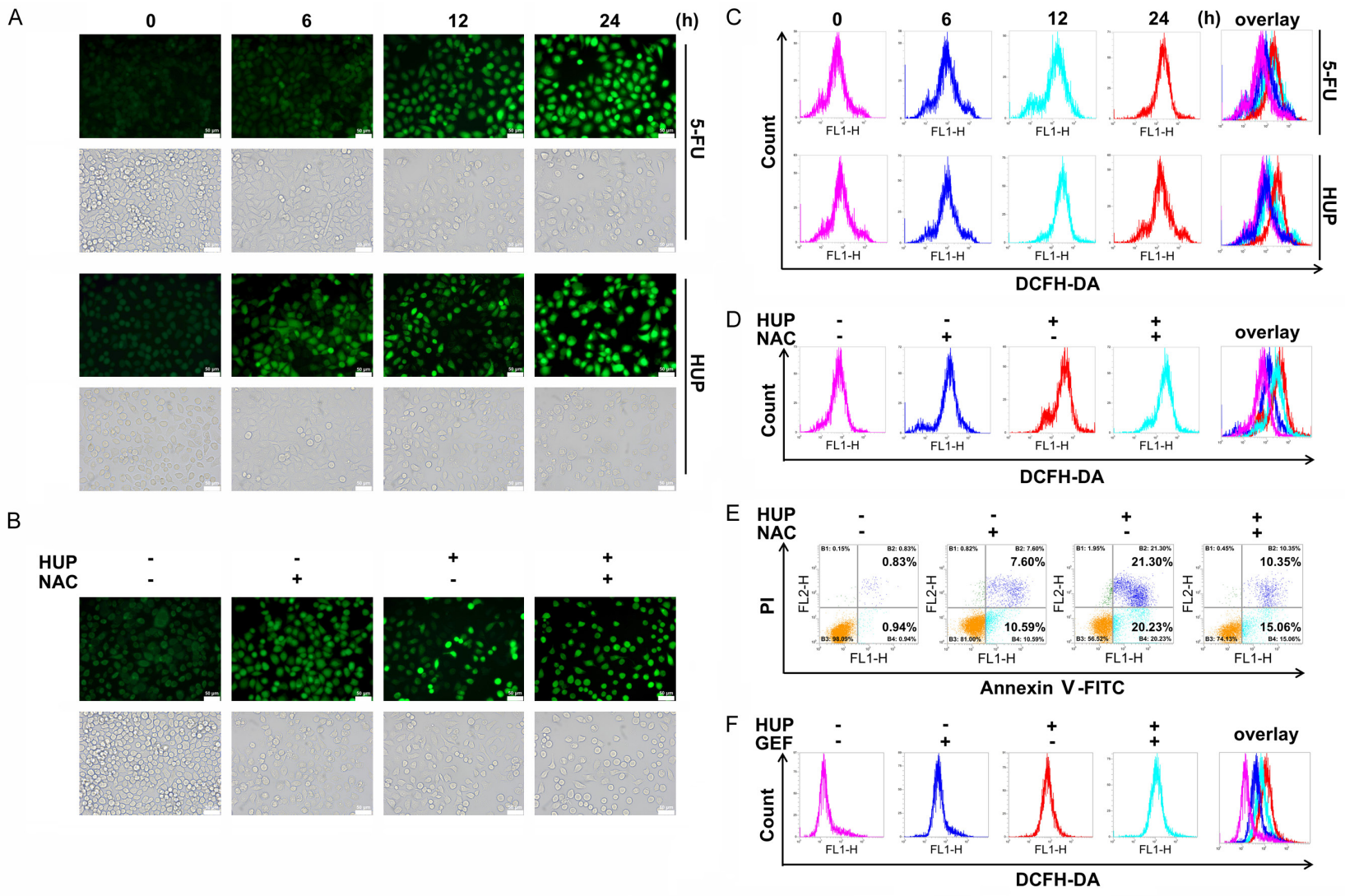
HUP arrested HepG2 cells in G0/G1 phase

A time-dependent decrease in the percentage of Ki67-positive cells was observed at 6, 12, and 24 h after HUP, suggesting an inhibition of cell proliferation (**Figure 5A**). According to flow cytometry analysis, HUP treatment substantially increased the percentage of cells within the G0/G1 phase, but decreased the S and G2/M phases over time (**Figure 5B**). The restoration of cell cycle distribution indicates that pre-treatment with the ROS scavenger NAC partially reversed HUP-induced G0/G1 arrest (**Figure 5C**).

Western blot analysis results indicated that HUP treatment decreased the levels of CDK2, CDK4, CDK6, cyclin D, and cyclin E in a time-dependent manner, concurrently increasing in the presentation of p21 and p27 (**Figure 5D**). NAC pre-treatment partially reversed the HUP-mediated changes in the cell cycle-related proteins (**Figure 5E**). Furthermore, treatment with the AKT inhibitor HY10249 showed changes in the expression of related proteins, indicating that these cell cycle regulators are downstream targets of the AKT pathway (**Figure 5F**). Collectively, HUP promotes G0/G1 phase detention within HepG2 cells through an ROS-dependent mechanism, indicating the involvement of the AKT pathway.

HUP suppressed the migration of HepG2 cells

HUP inhibits cell migration in a time-dependent manner (**Figure 6A**). Likewise, the wound healing assay indicated that HUP treatment progressively decreased in the wound closure rate (**Figure 6C**). Transwell and wound healing experiments showed that the administration of the ROS scavenger NAC before treatment partially mitigated the inhibitory effects of HUP on cell migration. Thus, ROS are involved in the


A
0
6
12
24
(h)
5-FU
HUP
B
HUP
NAC
C
overlay
Count
FL1-H
DCFH-DA
D
E
PI
FL2-H
0.83%
7.60%
21.30%
10.35%
0.94%
10.59%
20.23%
15.06%
Annexin V-FITC
F
GEF

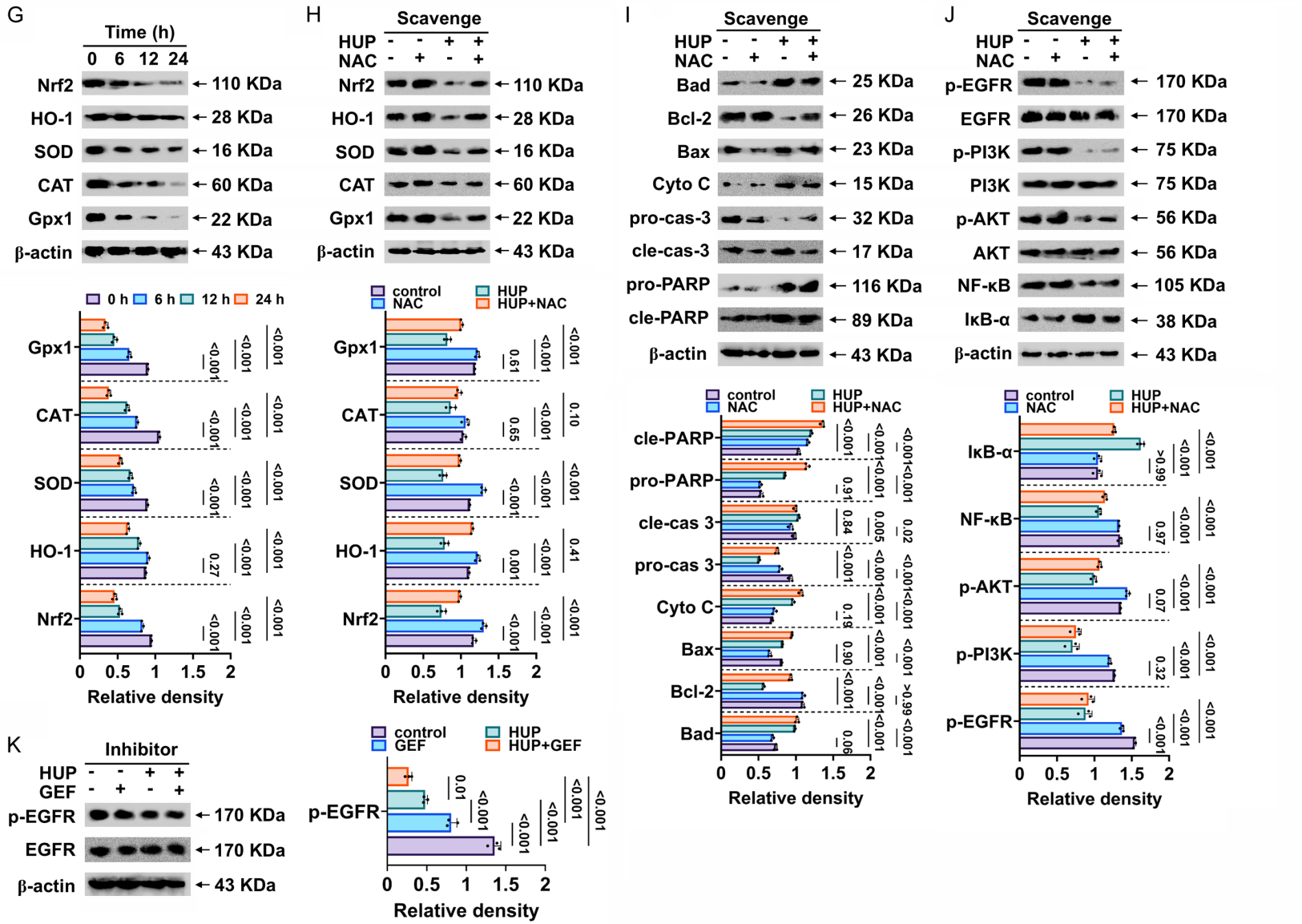
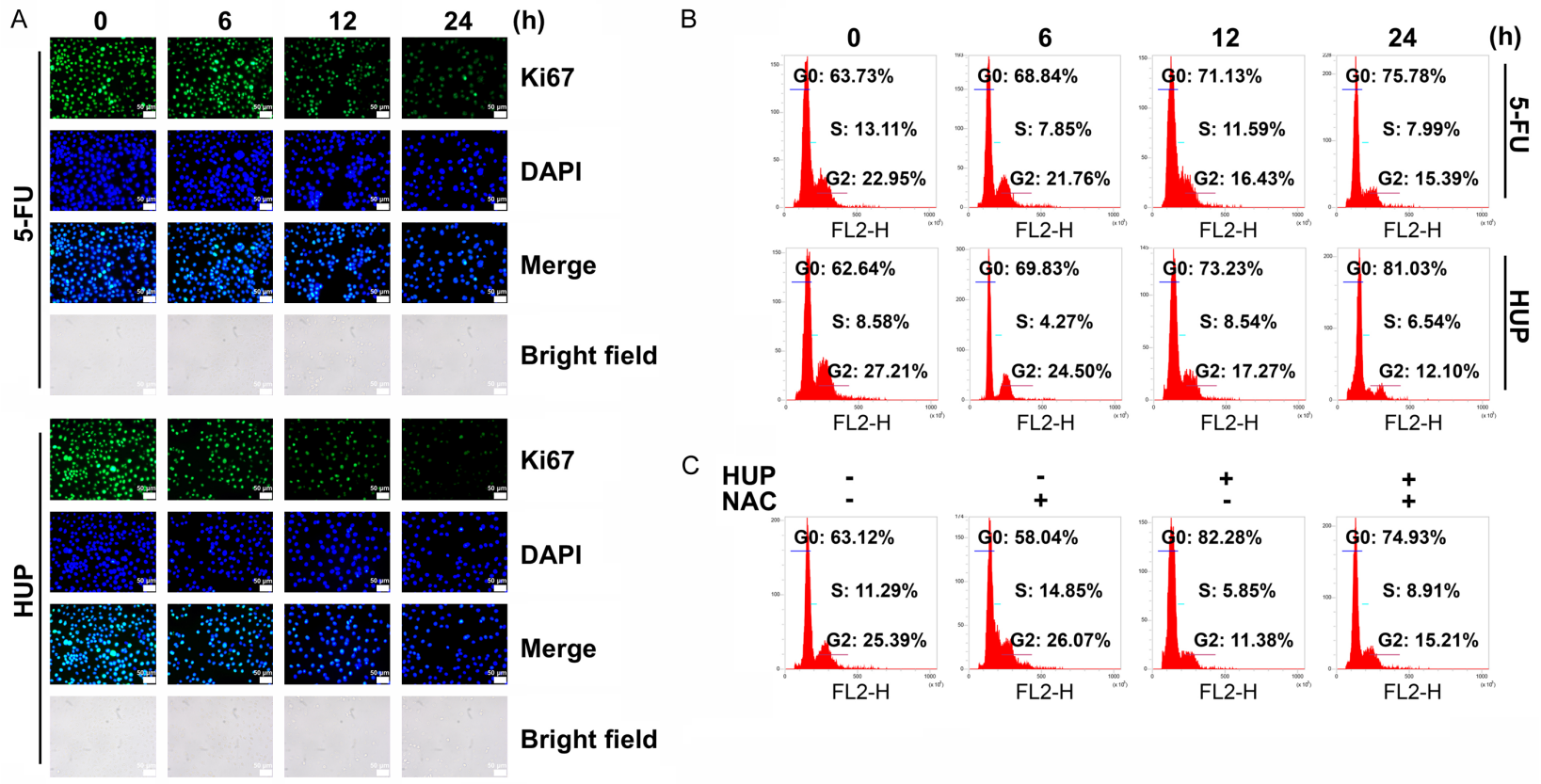

G
Time (h)
0 6 12 24
Nrf2 ← 110 KDa
HO-1 ← 28 KDa
SOD ← 16 KDa
CAT ← 60 KDa
Gpx1 ← 22 KDa
β-actin ← 43 KDa
0 h 6 h 12 h 24 h
Relative density
H
Scavenge
HUP
NAC
control
HUP
NAC
HUP+NAC
I
Bad ← 25 KDa
Bcl-2 ← 26 KDa
Bax ← 23 KDa
Cyto C ← 15 KDa
pro-cas-3 ← 32 KDa
cle-cas-3 ← 17 KDa
pro-PARP ← 116 KDa
cle-PARP ← 89 KDa
J
p-EGFR ← 170 KDa
EGFR ← 170 KDa
p-PI3K ← 75 KDa
PI3K ← 75 KDa
p-AKT ← 56 KDa
AKT ← 56 KDa
NF-κB ← 105 KDa
IκB-α ← 38 KDa
K
Inhibitor
GEF
GEF
HUP+GEF
p-EGFR ← 170 KDa
EGFR ← 170 KDa

Figure 4. Mechanism of reactive oxygen species (ROS)-Mediated oxidative stress and apoptosis in HepG2 cells. A. Changes in intracellular ROS levels in HepG2 cells treated with HUP or 5-FU for various durations (6, 12, and 24 h) were observed using 2',7'-dichlorodihydrofluorescein diacetate (DCFH-DA) staining. Scale bar: 50 μm. B. Effect of the ROS scavenger N-acetylcysteine (NAC) on HUP-induced ROS production in HepG2 cells, as determined by DCFH-DA staining. Scale bar: 50 μm. C. Quantitative analysis of changes in intracellular ROS levels in HepG2 cells treated with HUP or 5-FU for various durations (6, 12, and 24 h) using flow cytometry combined with DCFH-DA staining. D. Quantitative analysis of the effect of the ROS scavenger NAC on HUP-induced ROS production in HepG2 cells using flow cytometry combined with DCFH-DA staining. E. Quantitative analysis of the effect of the ROS scavenger NAC on HUP-induced apoptosis in HepG2 cells using flow cytometry combined with Annexin V-FITC/PI double staining. F. DCFH-DA-based flow cytometric analysis of intracellular ROS levels in HepG2 cells treated with HUP and/or the EGFR tyrosine kinase inhibitor gefitinib. G. Changes in the expression of antioxidant-related proteins (Nrf2, HO-1, SOD, CAT, and Gpx1) in HepG2 cells after HUP treatment for various durations (6, 12, and 24 h) were detected using western blotting. H. Western blot analysis of the effects of NAC pretreatment on HUP-induced changes in antioxidant-related proteins. I. Western blot analysis of the effects of NAC pretreatment on HUP-induced changes in apoptosis-related proteins. J. Western blot analysis of the effects of NAC pretreatment on HUP-induced changes in EGFR-PI3K-AKT and NF-κB pathway-related proteins. K. Western blot analysis of p-EGFR and total EGFR levels in HepG2 cells treated with HUP and/or gefitinib. *P* value indicate the statistical significance of the indicated pairwise comparisons. n = 3. magnification: 400×.



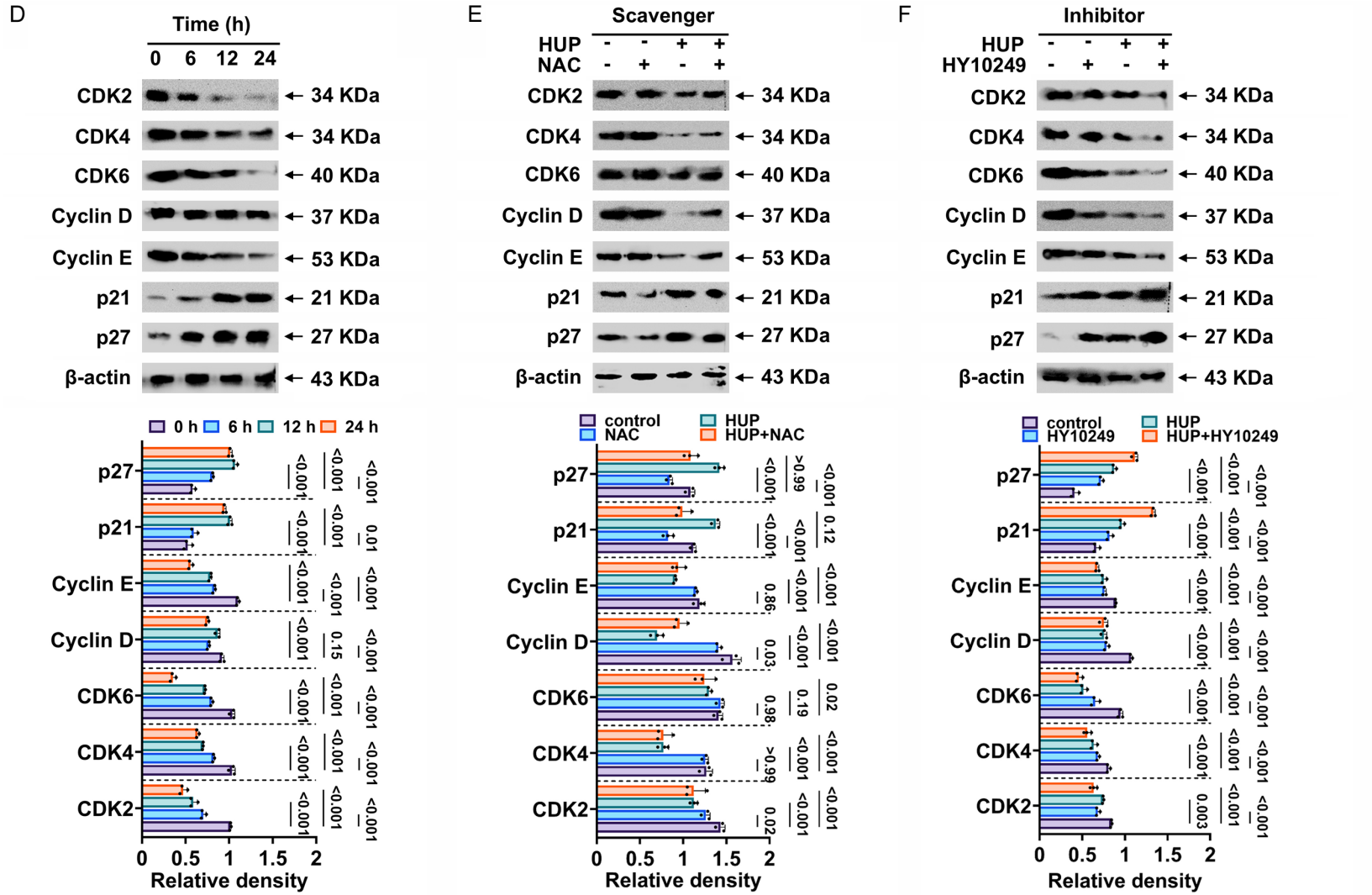


Figure 5. Mechanism of HUP-induced G0/G1 cell cycle arrest in HepG2 cells. A. Ki67/4',6-diamidino-2-phenylindole (DAPI) immunofluorescence staining was used to observe changes in the proliferative activity of HepG2 cells after treatment with HUP or 5-FU for different durations (6, 12, and 24 h). Scale bar: 50 μm. B. Flow cytometry analysis of changes in the cell cycle distribution of HepG2 cells after HUP or 5-FU treatment at different time points (6, 12, and 24 h). C. Flow cytometry was used to assess the reversal effect of the ROS scavenger NAC on HUP-induced cell cycle arrest in HepG2 cells. D. Western blotting was performed to detect changes in the expression levels of cell cycle-related proteins (CDK2, CDK4, CDK6, cyclin D, cyclin E, p21, and p27) in HepG2 cells after HUP treatment for various durations (6, 12, and 24 h). E. Western blotting was used to analyze the effect of NAC pre-treatment on the expression of cell cycle-related proteins regulated by HUP, verifying the upstream regulatory role of ROS in HUP-induced G0/G1 phase arrest. F. Western blot analysis of the effect of the AKT inhibitor HY10249 on the expression of cell cycle-related proteins in HepG2 cells verified the mechanism by which HUP regulates the cell cycle by inhibiting the AKT pathway. *P* value indicate the statistical significance of the indicated pairwise comparisons. n = 3. magnification: 400×.

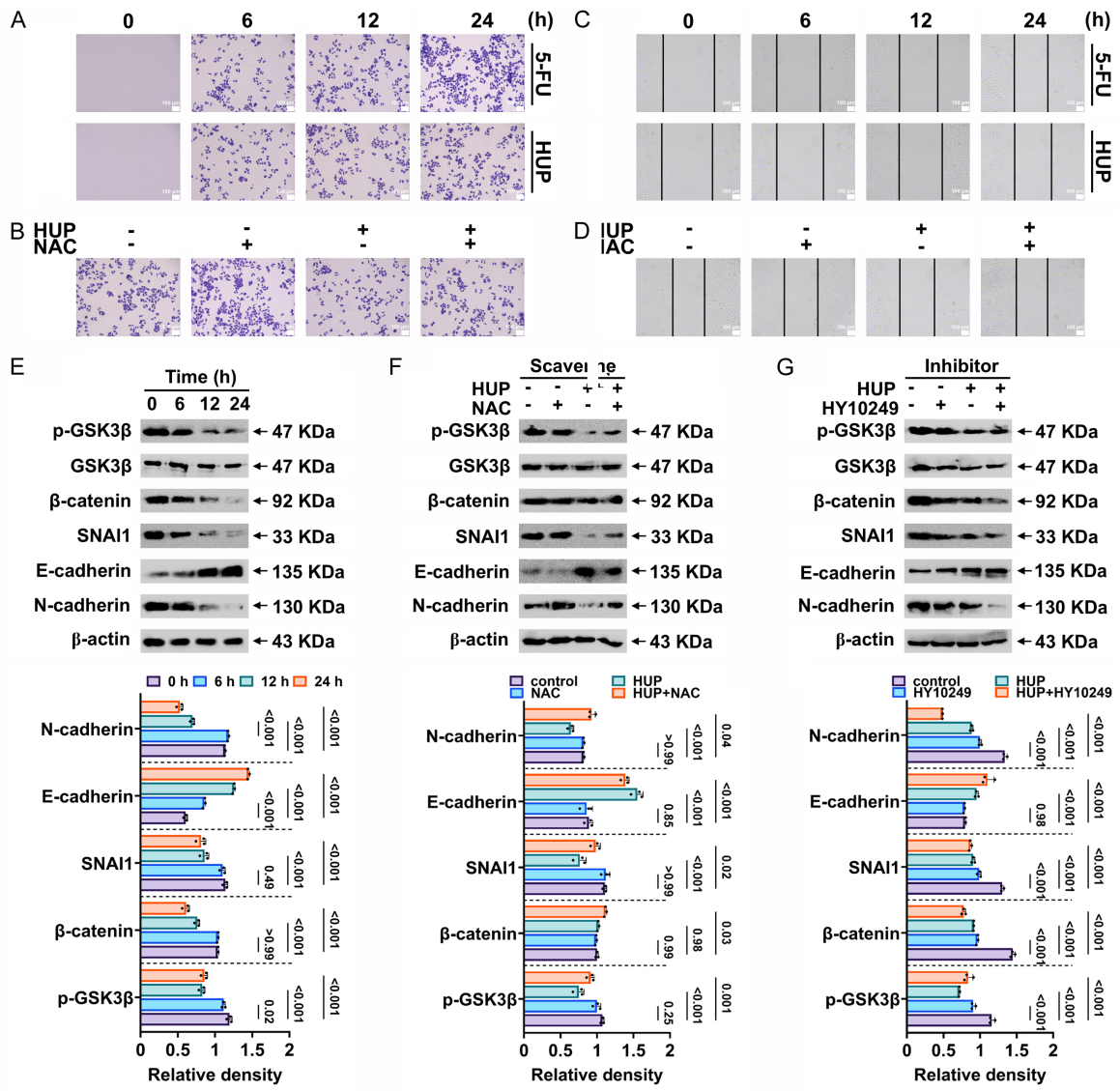


Figure 6. Mechanism of HUP inhibition of HepG2 cell migration via AKT-GSK-3β-β-catenin pathway. A. Transwell assay to detect changes in the in vitro migration ability of HepG2 cells after HUP or 5-FU treatment for different durations (0, 6, 12, and 24 h). Scale bar: 100 μm. B. Transwell assay examining the reversal effect of the ROS scavenger NAC on HUP-induced inhibition of HepG2 cell migration. Scale bar: 100 μm. C. Scratch wound healing assay to assess changes in the migratory ability of HepG2 cells after HUP or 5-FU treatment for different durations (6, 12, and 24 h). Scale bar: 100 μm. D. Scratch wound healing assay to examine the reversal effect of NAC on HUP-induced inhibition of HepG2 cell migration. Scale bar: 100 μm. E. Western blot analysis of epithelial-mesenchymal transition (EMT)-related protein expression (p-glycogen synthase kinase 3 beta (GSK-3β), GSK3β, β-catenin, Snail family transcriptional repressor 1 (SNAI1), E-cadherin, and N-cadherin) in HepG2 cells after HUP treatment for different durations (6, 12, and 24 h). F. Western blot analysis to detect the reversal effect of NAC pre-treatment on HUP-regulated EMT-related and pathway proteins, verifying the upstream role of ROS in HUP-mediated regulation of EMT. G. Western blot analysis was performed to examine the effect of the AKT inhibitor HY10249 on the expression of EMT-related proteins and pathway proteins in HepG2 cells, verifying the mechanism by which HUP regulates EMT by inhibiting the AKT/GSK3β pathway. *P* value indicate the statistical significance of the indicated pairwise comparisons. n = 3. magnification: 100×.

HUP-induced migratory decrease (**Figure 6B** and **6D**).

Western blotting was conducted to analyze the proteins associated with EMT. HUP treatment decreased p-GSK-3β, β-catenin, SNAI1, and N-cadherin levels in a time-dependent manner, while increasing E-cadherin expression (**Figure 6E**). NAC pre-treatment partially reversed the HUP-induced changes in EMT-related protein

expression (**Figure 6F**). Furthermore, treatment with the AKT inhibitor mirrored the effects of HUP on EMT-related proteins, indicating that HUP inhibits EMT via the AKT/GSK-3β pathway (**Figure 6G**). Collectively, HUP suppresses HepG2 cell migration by inhibiting EMT in an ROS-dependent manner through the AKT/GSK-3β pathway.

HUP inhibits xenograft tumor growth

Figure 7A displays the modeling and administration protocols. After the completion of modeling, nude mice received HUP for 16 days and were humanely killed. The representative nude mice from the experimental group were compared with the tumor (**Figure 7B**). HUP treatment reduced tumor growth in a dose-dependent manner, with the HUP 50 mg/kg group showing the smallest tumor volume at the end of the treatment period. The tumor volume (496 mm^3) and weight (1.25 g) in the vehicle group were approximately 1.5 times and 2.0 times those in the 5-FU group (320 mm^3, 0.62 g), whereas approximately 3.1 times and 7.8 times those of the HUP 50 mg/kg treatment group (159 mm^3, 0.16 g), respectively (**Figure 7C** and **7D**). Nude mice showed normal body weight with transplanted tumors, complete five main organs, and smooth surfaces without visible pathological changes (**Figure 7E** and **7F**). In comparison to the Normal group, the Vehicle model group exhibited significantly increased indices for the liver, kidney, and spleen. HUP treatment reduced the abnormal increases in these organ indices (**Figure 7G-I**).

H&E staining further confirmed that HUP treatment did not cause significant histopathological damage in the major organs of nude mice, indicating tolerable safety (**Figure 7J**). Immunohistochemical analysis of tumor tissues was conducted to clarify the underlying in vivo mechanisms. HUP treatment led to a dose-dependent decrease in the presentation of p-EGFR, p-PI3K, and p-AKT. Concurrently, increased levels of cleaved caspase-3 and cleaved PARP indicated the activation of apoptotic signaling in tumor tissues (**Figure 7K**). Thus, HUP effectively restricts the growth of HepG2 xenografts by inhibiting the EGFR-PI3K-AKT pathway while triggering apoptosis. Additionally, it has a safe profile without noticeable adverse effects on major organs.

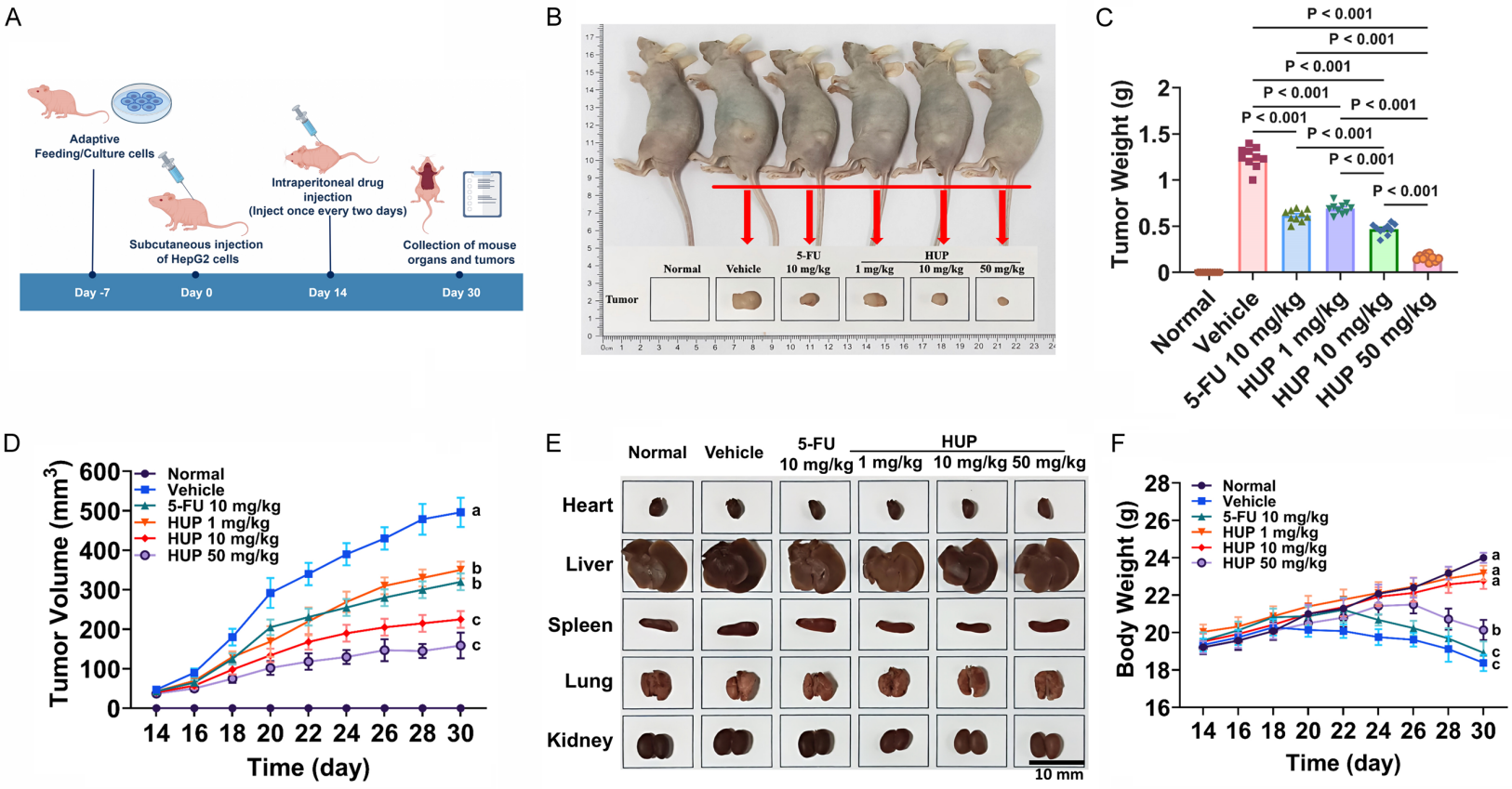
Discussion

High intra- and inter-tumor heterogeneity results in increased rates of chemotherapy resistance [29]. Although the pharmacological efficacy of Traditional Chinese medicine is recorded in ancient literature, comprehensive verification of its mechanism of action is lacking [30]. HUP, a natural isosteroidal alkaloid, is extracted from *Fritillaria hupehensis* [31]. Owing to their extensive use in both traditional and modern medicine, alkaloids, a class of natural compounds with a wide range of pharmacological activities, are ideal for drug discovery [32, 33].

For the first time, this research shows that HUP exhibits significant anti-HCC efficacy in both in vitro and in vivo settings. HUP exhibited comparable or superior activity to other anti-HCC natural products. For instance, the well-known alkaloid berberine demonstrated antitumor activity by triggering apoptosis and stopping the cell cycle in HepG2 cells, with IC_{50} values ranging from 25.01 μM to 39.99 μM. However, HUP had an IC_{50} value of 10.38 μM for HepG2 cells [34]. This suggests that HUP warrants further pharmacological investigation.

Notably, 5,6-anhydrohupehenine, a new isosteroidal alkaloid isolated from *Fritillaria hupehensis*, had an IC_{50} of 12.21 μM against HepG2 cells, and its activity was marginally lower than that of HUP. Nevertheless, its key derivative 9s exhibited the strongest inhibitory activity against HepG2 cells, with an IC_{50} of 1.27 μM [35]. Therefore, there is sufficient room for structural optimization in the intrinsically more active HUP skeleton, and future chemical modifications may be further investigated.

Instead of using 5-FU as a mechanistic comparator, this study used it as a positive control to compare antitumor efficacy. 5-FU is a classical fluoropyrimidine antimetabolite that primarily inhibits thymidylate synthase and incorporates its metabolites into RNA and DNA to produce anticancer effects [36]. In contrast, the present results suggest that HUP exerts anti-HCC effects through EGFR signaling suppression, ROS accumulation, downstream inhibition of PI3K/AKT signaling, mitochondrial apoptosis, cell-cycle arrest, and cell migration inhibition. Despite these mechanistic differences, HUP exhibited antitumor activity comparable to


A
Adaptive
Feeding/Culture cells
Subcutaneous injection
of HepG2 cells
Intraperitoneal drug
injection
(Inject once every two days)
Collection of mouse
organs and tumors
Day -7
Day 0
Day 14
Day 30
B
Normal
Vehicle
5-FU
10 mg/kg
HUP
1 mg/kg
10 mg/kg
50 mg/kg
Tumor
C
P < 0.001
Tumor Weight (g)
Normal
Vehicle
5-FU 10 mg/kg
HUP 1 mg/kg
HUP 10 mg/kg
HUP 50 mg/kg
D
Tumor Volume (mm3)
Time (day)
Normal
Vehicle
5-FU 10 mg/kg
HUP 1 mg/kg
HUP 10 mg/kg
HUP 50 mg/kg
E
Heart
Liver
Spleen
Lung
Kidney
10 mm
F
Body Weight (g)
Time (day)

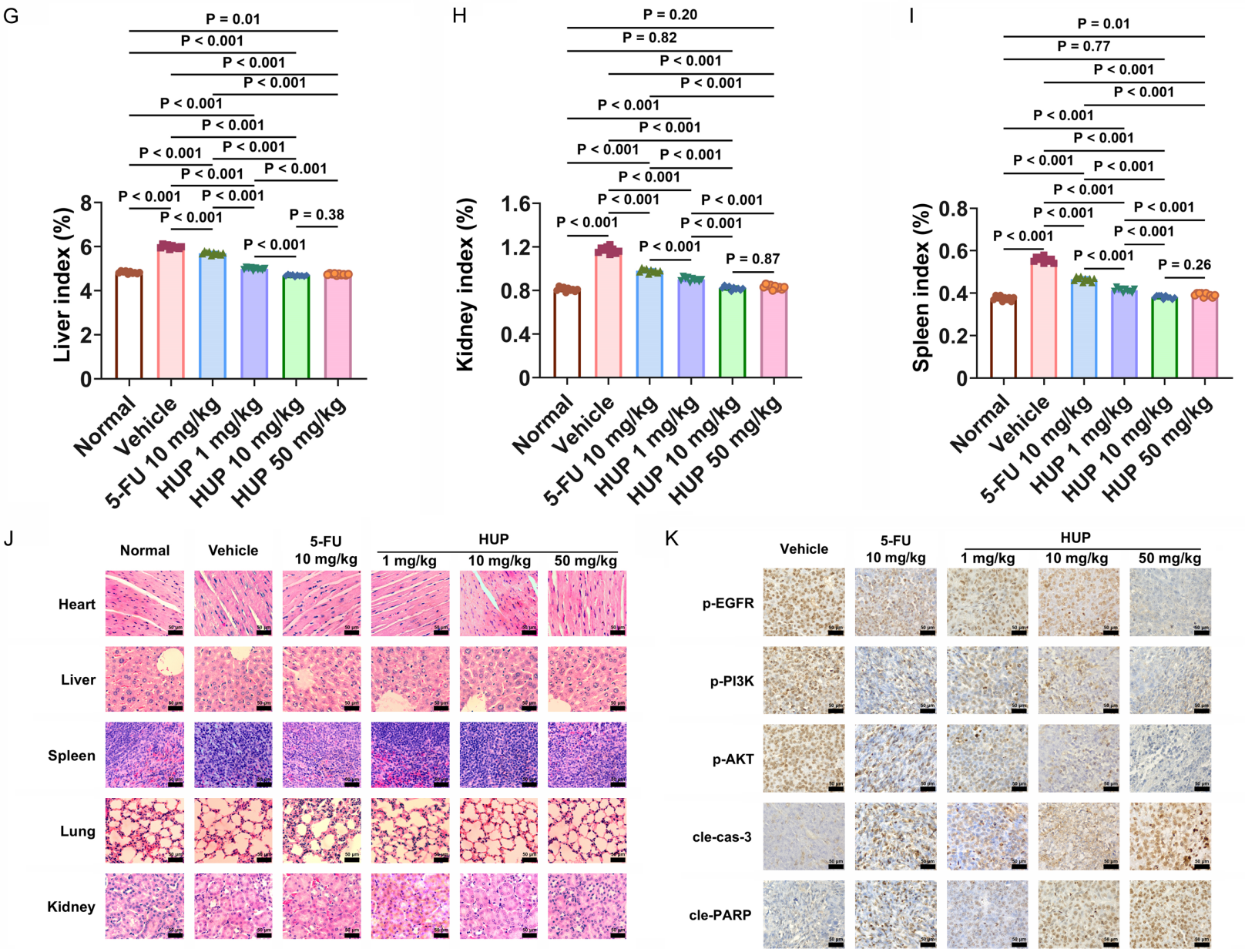

G
Liver index (%)
P = 0.01
P < 0.001
P < 0.001
P < 0.001
P < 0.001
P < 0.001
P < 0.001
P < 0.001
P < 0.001
P < 0.001
P < 0.001
P < 0.001
P = 0.38
P < 0.001
Normal
Vehicle
5-FU 10 mg/kg
HUP 1 mg/kg
HUP 10 mg/kg
HUP 50 mg/kg
H
Kidney index (%)
P = 0.20
P = 0.82
P < 0.001
P < 0.001
P < 0.001
P < 0.001
P < 0.001
P < 0.001
P < 0.001
P < 0.001
P < 0.001
P < 0.001
P < 0.001
P < 0.001
P = 0.87
I
Spleen index (%)
P = 0.01
P = 0.77
P < 0.001
P < 0.001
P < 0.001
P < 0.001
P < 0.001
P < 0.001
P < 0.001
P < 0.001
P < 0.001
P < 0.001
P < 0.001
P < 0.001
P = 0.26
J
Normal
Vehicle
5-FU 10 mg/kg
HUP
1 mg/kg
10 mg/kg
50 mg/kg
Heart
Liver
Spleen
Lung
Kidney
K
Vehicle
5-FU 10 mg/kg
HUP
1 mg/kg
10 mg/kg
50 mg/kg
p-EGFR
p-PI3K
p-AKT
cle-cas-3
cle-PARP

Figure 7. HUP suppresses HepG2 tumor growth and demonstrates favorable safety in a nude mouse xenograft model. (A) Schematic representation of the establishment of a subcutaneous HepG2 xenograft tumor model in nude mice and experimental drug administration. (B) Photographs of representative nude mice and excised subcutaneous xenograft tumors from each group. (C) Statistical analysis of tumor weights in each group of nude mice. (D) Growth curves of tumor volume over time in each group of nude mice. (E) Observation of major organs (heart, liver, spleen, lung, and kidney) in each group of nude mice. Scale bar: 10 mm. (F) Curve analysis of body weight changes in nude mice during the modeling process in each group. (G-I) Liver, kidney, and spleen index analysis of nude mice in each experimental group. *P*-values between the indicated two groups were marked above the corresponding column bars. (J) Histopathological observation of major organs in each group of nude mice by HE staining. Scale bar: 50 μm. (K) Immunohistochemical detection of protein expression levels of p-EGFR, p-PI3K, p-AKT, cleaved caspase-3, and cleaved PARP in tumor tissues of each group of nude mice. Scale bar: 50 μm. *P* value in (C) and (G-I) indicate the statistical significance of the indicated pairwise comparisons. Different lowercase letters in (D) and (F) indicate significant differences between groups at the final time point ($P < 0.05$). Tumor volume and organ index data are presented as mean ± SEM. Tumor volume (D) and body weight (F) were analyzed using two-way repeated-measures ANOVA with Greenhouse-Geisser correction. n = 10/group. magnification: 400×.

or higher than that of 5-FU. Moreover, HUP exerted minimal effects on the healthy cell lines, suggesting a favorable selectivity profile.

At the mechanistic level, HUP-induced apoptosis was characterized by the loss of mitochondrial membrane potential, changes in Bcl-2 family protein expression, cytochrome c release, and activation of caspase-3 and PARP, which corroborate the induction of mitochondrial apoptosis [37]. HUP increased ROS levels in HepG2 cells and decreased the expression of Nrf2 and its downstream antioxidant-related proteins, such as HO-1, SOD, CAT, and Gpx1. Therefore, the disruption of the Nrf2-related antioxidant defense system may contribute to oxidative stress. Nonetheless, the precise temporal and causal relationship remains to be clarified. Isosteroidal alkaloids from *Fritillaria hupehensis* protect macrophages from oxidative stress damage by triggering the Nrf2/HO-1 pathway [38, 39]. In contrast, HUP suppresses this axis in HepG2 cells to promote ROS-mediated apoptosis. This differential regulation suggests that the impact of HUP on redox signaling may depend on the cell type, providing a mechanistic explanation for its selective cytotoxicity toward HCC cells.

To further clarify the relationship between EGFR and ROS, NAC and gefitinib intervention experiments were conducted. NAC did not restore HUP-induced EGFR phosphorylation, whereas gefitinib-mediated EGFR inhibition increased intracellular ROS. Thus, ROS acts downstream of EGFR and contributes to PI3K/AKT regulation. HUP decreased CDK2/4/6 and cyclin D/E levels while increasing p21/p27 levels, leading to the arrest of HepG2 cells in the G0/G1 phase. Berberine induces G0/G1 arrest in HCC cells through AKT inhibition. However, the downstream mechanism involves the AKT/FoxO3a/Skp2 axis [40]. Both HUP and berberine can induce cell cycle arrest through the AKT/p21/p27 pathway; however, HUP affects the upstream pathways, highlighting the differences between these alkaloids during signal transduction.

In vivo xenograft tumor experiments further evaluated the antitumor activity and short-term tolerability of HUP. HUP did not cause significant weight loss or damage to the heart, liver, spleen, lungs, or kidneys. H&E staining and immunohistochemistry further confirmed that HUP reduced p-EGFR, p-PI3K, and p-AKT expression while upregulating cleaved caspase-3 and cleaved PARP in vivo. This finding supports its mechanism of inducing apoptosis in HepG2 cells through the EGFR-PI3K-AKT pathway. In summary, HUP exerted consistent regulatory effects on EGFR-PI3K-AKT signaling and short-term tolerability in vivo, supporting further investigation of the anti-HCC potential of HUP.

Although molecular docking predicted potential interactions between HUP and EGFR or AKT1, direct physical binding was not experimentally established. The pharmacological intervention experiments support the involvement of EGFR signaling in the cellular response to HUP, whereas direct target engagement remains to be further validated using biophysical or target-engagement approaches. Accordingly, EGFR is interpreted here as a pharmacologically implicated signaling node rather than an experimentally established direct molecular target of

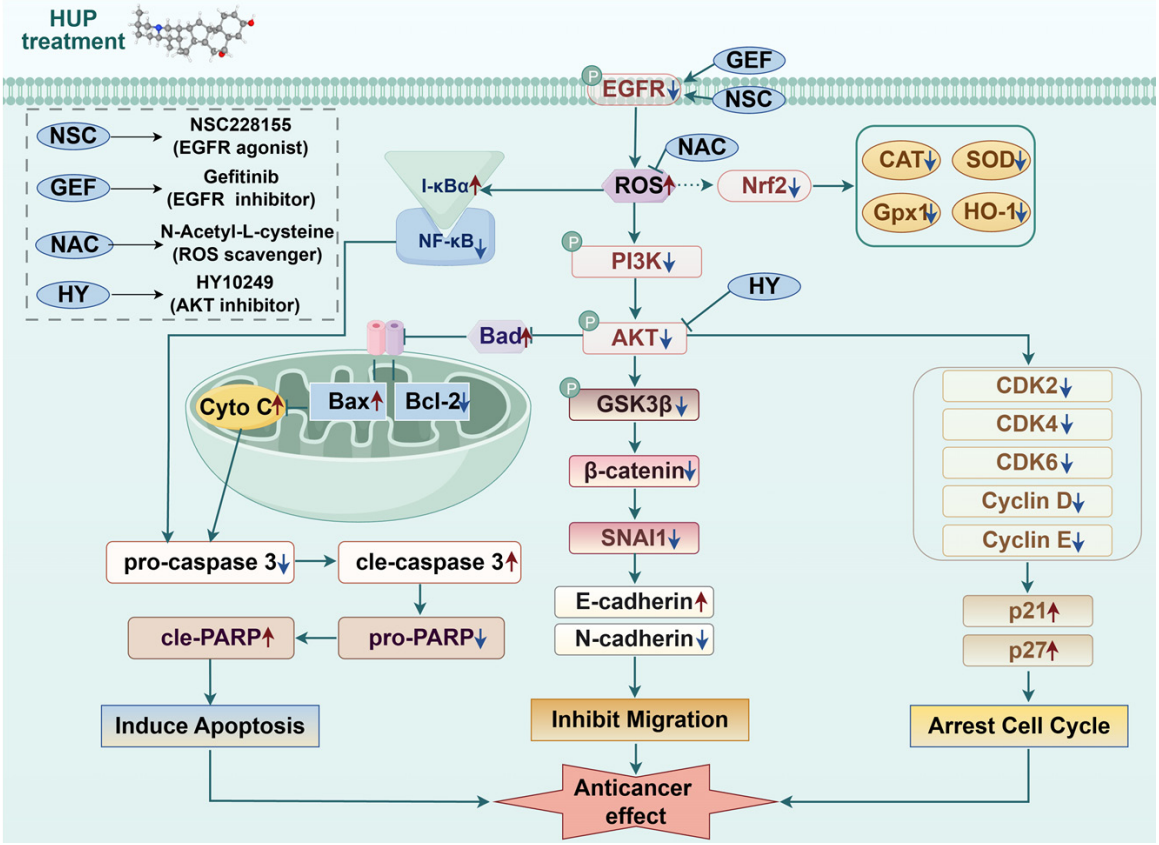


Figure 8. Schematic summary of signaling changes associated with the anti-HCC effects of HUP. HUP treatment was associated with reduced EGFR phosphorylation, increased intracellular ROS accumulation, and suppression of downstream PI3K-AKT signaling. These changes were accompanied by mitochondrial apoptosis, G0/G1 cell-cycle arrest, and inhibition of EMT-related cell migration. Pharmacological interventions with the EGFR agonist NSC228155, EGFR inhibitor gefitinib, ROS scavenger N-acetylcysteine (NAC), and AKT inhibitor HY10249 were used to further investigate these signaling relationships.

HUP. Additional concentration-response experiments at 6 h showed concentration-related changes in ROS, EGFR phosphorylation, and AKT phosphorylation. Notably, AKT phosphorylation was reduced at 2.5 μM HUP, a concentration that did not significantly affect cell viability, reducing the possibility that these signaling changes were solely secondary to extensive cell death. Additionally, pharmacokinetic parameters, including plasma and tumor exposure, metabolic stability, clearance, and PK/PD relationships, were not investigated. Moreover, its long-term safety and efficacy in immunocompetent animal models are unclear. Nevertheless, the in vitro and in vivo findings support the anti-HCC activity of HUP, necessitating additional mechanistic and pharmacological investigation. Future studies should further characterize the pharmacological properties of HUP and validate its direct molecular targets.

Conclusions

HUP exhibited strong anti-HCC activity associated with the suppression of EGFR signaling, ROS accumulation, and downstream inhibition of PI3K-AKT signaling. These changes were accompanied by mitochondrial apoptotic responses, G0/G1 cell-cycle arrest, and the inhibition of HepG2 cell migration. In vivo investigations have substantiated its antitumor effectiveness and short-term tolerability under the tested conditions. Thus, these findings support further preclinical investigation of HUP in HCC (**Figure 8**).

Acknowledgements

We acknowledge Figdraw (www.figdraw.com) for providing an illustration platform for our **Figures 7A** and **8**. We also thank MogoEdit (www.mogoedit.com) for professional English-

language editing. This research was supported by the Heilongjiang Province Key Research and Development Plan Guidance Project (grant no. GZ20220039), the Central Government Supports Local College Reform and Development Fund Talent Training Project (grant no. 2020GSP16), the National Natural Science Foundation of China (grant no. 82460126), and the Program for Young Talents of Science and Technology in Universities of Inner Mongolia Autonomous Region (grant no. NJYT24032), the "Three Verticals" Scientific Research Support Program Projects (grant no. ZRCPY202318), and the Postgraduate Innovative Research Project of Heilongjiang Bayi Agricultural University (grant no. YJSCX2025-KJQN66).

Disclosure of conflict of interest

None.

Address correspondence to: Cheng-Hao Jin, Department of Biochemistry and Molecular Biology, College of Life Science and Biotechnology, Heilongjiang Bayi Agricultural University, No. 5 Xinfeng Road, Daqing 163319, Heilongjiang, China. E-mail: jinchenghao3727@byau.edu.cn; Tian-Zhu Li, Department of Molecular Biology, College of Basic Medical Science, Chifeng University, No. 60 Tiedanan Street, Hongshan District, Chifeng 024000, Inner Mongolia Autonomous Region, China. E-mail: litianzhu@cfxy.edu.cn

References

[1] Bray F, Laversanne M, Sung H, Ferlay J, Siegel RL, Soerjomataram I and Jemal A. Global cancer statistics 2022: GLOBOCAN estimates of incidence and mortality worldwide for 36 cancers in 185 countries. CA Cancer J Clin 2024; 74: 229-263.

[2] Gomaa AI, Khan SA, Toledano MB, Waked I and Taylor-Robinson SD. Hepatocellular carcinoma: epidemiology, risk factors and pathogenesis. World J Gastroenterol 2008; 14: 4300-4308.

[3] Young EG, Li FF and Brimble MA. Spiroketal natural products isolated from traditional Chinese medicine: isolation, biological activity, biosynthesis, and synthesis. Nat Prod Rep 2025; 42: 1786-1810.

[4] Chopra B and Dhingra AK. Natural products: a lead for drug discovery and development. Phytother Res 2021; 35: 4660-4702.

[5] Luo H, Vong CT, Chen H, Gao Y, Lyu P, Qiu L, Zhao M, Liu Q, Cheng Z, Zou J, Yao P, Gao C, Wei J, Ung COL, Wang S, Zhong Z and Wang Y. Naturally occurring anti-cancer compounds: shining from Chinese herbal medicine. Chin Med 2019; 14: 48.

[6] Duan Y, Liu X, Wu J, You J, Wang F, Guo X, Tang T, Liao M and Guo J. Transcriptomic and metabolic analyses reveal the potential mechanism of increasing steroidal alkaloids in Fritillaria hupehensis through intercropping with Magnolia officinalis. Front Plant Sci 2022; 13: 997868.

[7] Gao YQ, Zhang LX, Wang MR and Song B. Pollination biology of Fritillaria delavayi. Zhongguo Zhong Yao Za Zhi 2014; 39: 1795-1798.

[8] Gao Y, Wang C, Song B and Du F. Corolla retention after pollination facilitates the development of fertilized ovules in Fritillaria delavayi (Liliaceae). Sci Rep 2019; 9: 729.

[9] Elmore S. Apoptosis: a review of programmed cell death. Toxicol Pathol 2007; 35: 495-516.

[10] Tuzlak S, Kaufmann T and Villunger A. Interrogating the relevance of mitochondrial apoptosis for vertebrate development and postnatal tissue homeostasis. Genes Dev 2016; 30: 2133-2151.

[11] Sun W, Zhang ND, Zhang T, Li YN, Xue H, Cao JL, Hou WS, Liu J, Wang Y and Jin CH. Cyanidin-3-O-glucoside induces the apoptosis of human gastric cancer MKN-45 cells through ROS-mediated signaling pathways. Molecules 2023; 28: 652.

[12] Cao J, Li S, Zhang T, Liu J, Hou W, Wang A, Wang C and Jin C. Valtrate exerts anticancer effects on gastric cancer AGS cells by regulating reactive oxygen species-mediated signaling pathways. Biocell 2024; 48: 313-325.

[13] Li Y, Zhu J, Yu Z, Zhai F, Li H and Jin X. Regulation of apoptosis by ubiquitination in liver cancer. Am J Cancer Res 2023; 13: 4832-4871.

[14] Reed JC. Bcl-2 family proteins. Oncogene 1998; 17: 3225-3236.

[15] Kuwana T and Newmeyer DD. Bcl-2-family proteins and the role of mitochondria in apoptosis. Curr Opin Cell Biol 2003; 15: 691-699.

[16] Hu W, Fu J, Lu SX, Liu LL, Luo RZ, Yun JP and Zhang CZ. Decrease of Bcl-xL/Bcl-2-associated death promoter in hepatocellular carcinoma indicates poor prognosis. Am J Cancer Res 2015; 5: 1805-1813.

[17] Sahoo BM, Banik BK, Borah P and Jain A. Reactive oxygen species (ROS): key components in cancer therapies. Anticancer Agents Med Chem 2022; 22: 215-222.

[18] Zhang H, Sun K, Gao M and Xu S. Zinc inhibits lead-induced oxidative stress and apoptosis of ST cells through ROS/PTEN/PI3K/AKT axis. Biol Trace Elem Res 2024; 202: 980-989.

[19] Ge Q, Yan Z, Tian Q, Zhang J, Li J, Cai F, Zhang L and Zhu Y. Xanthohumol regulates mitopha-

gy in osteosarcoma cells via AMPK-ULK1-FUNDC1 signaling pathway. Phytother Res 2025; 39: 2393-2406.
[20] Liu H, Liang S, Peng C, Yang J, Yang Z and Mo W. NSUN3-mediated ROS accumulation promotes hepatocellular carcinoma proliferation and activates PI3K/AKT pathway. Biochem Genet 2026; 64: 2782-2796.
[21] Salehi B, Zucca P, Sharifi-Rad M, Pezzani R, Rajabi S, Setzer WN, Varoni EM, Iriti M, Kobarfard F and Sharifi-Rad J. Phytotherapeutics in cancer invasion and metastasis. Phytother Res 2018; 32: 1425-1449.
[22] Clarke CA, Hubbell E, Kurian AW, Colditz GA, Hartman AR and Gomez SL. Projected reductions in absolute cancer-related deaths from diagnosing cancers before metastasis, 2006-2015. Cancer Epidemiol Biomarkers Prev 2020; 29: 895-902.
[23] Bittner KR, Jiménez JM and Peyton SR. Vascularized biomaterials to study cancer metastasis. Adv Healthc Mater 2020; 9: e1901459.
[24] Xue TC, Ge NL, Zhang L, Cui JF, Chen RX, You Y, Ye SL and Ren ZG. Goosecoid promotes the metastasis of hepatocellular carcinoma by modulating the epithelial-mesenchymal transition. PLoS One 2014; 9: e109695.
[25] Bai J, Kwok WC and Thiery JP. Traditional Chinese medicine and regulatory roles on epithelial-mesenchymal transitions. Chin Med 2019; 14: 34.
[26] Yan Y, Li G, Tian X, Ye Y, Gao Z, Yao J, Zhang F and Wang S. Ischemic preconditioning increases GSK-3β/β-catenin levels and ameliorates liver ischemia/reperfusion injury in rats. Int J Mol Med 2015; 35: 1625-1632.
[27] Sheng T, Su H, Yao L, Qu Z, Liu H, Shao W and Zhang X. RhoB regulates prostate cancer cell proliferation and docetaxel sensitivity via the PI3K-AKT signaling pathway. BMC Cancer 2025; 25: 354.
[28] Ma Z, Lou S and Jiang Z. PHLDA2 regulates EMT and autophagy in colorectal cancer via the PI3K/AKT signaling pathway. Aging (Albany NY) 2020; 12: 7985-8000.
[29] Bai L, Yan X, Lv J, Qi P, Song X and Zhang L. Intestinal flora in chemotherapy resistance of biliary pancreatic cancer. Biology (Basel) 2023; 12: 1151.
[30] Wang Y, Liu H, Dai S, Sun W and Ren N. Multitarget mechanisms and clinical integration of traditional Chinese medicine in breast cancer. Phytomedicine 2026; 155: 158090.
[31] Duan Y, Wu J, Wang F, Zhang K, Guo X, Tang T, Mu S, You J and Guo J. Transcriptomic and metabolomic analyses provide new insights into the appropriate harvest period in regenerated bulbs of Fritillaria hupehensis. Front Plant Sci 2023; 14: 1132936.
[32] Bhambhani S, Kondhare KR and Giri AP. Diversity in chemical structures and biological properties of plant alkaloids. Molecules 2021; 26: 3374.
[33] Liu C, Yang S, Wang K, Bao X, Liu Y, Zhou S, Liu H, Qiu Y, Wang T and Yu H. Alkaloids from traditional Chinese medicine against hepatocellular carcinoma. Biomed Pharmacother 2019; 120: 109543.
[34] K S, Karan Chand Mohan Singh S, Boopathi S, Pichamuthu SP, I N and R G. A systematic review with targeted meta-analyses of curcumin and berberine in vitro cytotoxicity models (2014-2026). Cureus 2026; 18: e104165.
[35] Liu XH, Zou J, Li YJ, Liu M, He CL, Liu YR, Wang JZ and Chen DL. Isosteroidal alkaloids from Fritillaria hupehensis Hsiao et K.C.Hsia: synthesis and biological evaluation of alkaloid derivatives as potential cytotoxic agents. Steroids 2021; 176: 108929.
[36] Longley DB, Harkin DP and Johnston PG. 5-fluorouracil: mechanisms of action and clinical strategies. Nat Rev Cancer 2003; 3: 330-338.
[37] Tait SW and Green DR. Mitochondrial regulation of cell death. Cold Spring Harb Perspect Biol 2013; 5: a008706.
[38] Galluzzi L, Vitale I, Aaronson SA, Abrams JM, Adam D, Agostinis P, Alnemri ES, Altucci L, Amelio I, Andrews DW, Annicchiarico-Petruzzelli M, Antonov AV, Arama E, Baehrecke EH, Barlev NA, Bazan NG, Bernassola F, Bertrand MJM, Bianchi K, Blagosklonny MV, Blomgren K, Borner C, Boya P, Brenner C, Campanella M, Candi E, Carmona-Gutierrez D, Cecconi F, Chan FK, Chandel NS, Cheng EH, Chipuk JE, Cidlowski JA, Ciechanover A, Cohen GM, Conrad M, Cubillos-Ruiz JR, Czabotar PE, D'Angiolella V, Dawson TM, Dawson VL, De Laurenzi V, De Maria R, Debatin KM, DeBerardinis RJ, Deshmukh M, Di Daniele N, Di Virgilio F, Dixit VM, Dixon SJ, Duckett CS, Dynlacht BD, El-Deiry WS, Elrod JW, Fimia GM, Fulda S, García-Sáez AJ, Garg AD, Garrido C, Gavathiotis E, Golstein P, Gottlieb E, Green DR, Greene LA, Gronemeyer H, Gross A, Hajnoczky G, Hardwick JM, Harris IS, Hengartner MO, Hetz C, Ichijo H, Jäättelä M, Joseph B, Jost PJ, Juin PP, Kaiser WJ, Karin M, Kaufmann T, Kepp O, Kimchi A, Kitsis RN, Klionsky DJ, Knight RA, Kumar S, Lee SW, Lemasters JJ, Levine B, Linkermann A, Lipton SA, Lockshin RA, López-Otín C, Lowe SW, Luedde T, Lugli E, MacFarlane M, Madeo F, Malewicz M, Malorni W, Manic G, Marine JC, Martin SJ, Martinou JC, Medema JP, Mehlen P, Meier P, Melino S, Miao EA, Molkentin JD, Moll UM, Muñoz-Pinedo C, Nagata S, Nuñez G, Oberst A, Oren M, Overholtzer M, Pagano M, Panaretakis T, Pasparakis M, Penninger JM, Pereira DM, Pervaiz S, Peter ME, Piacentini M, Pinton P, Prehn

JHM, Puthalakath H, Rabinovich GA, Rehm M, Rizzuto R, Rodrigues CMP, Rubinsztein DC, Rudel T, Ryan KM, Sayan E, Scorrano L, Shao F, Shi Y, Silke J, Simon HU, Sistigu A, Stockwell BR, Strasser A, Szabadkai G, Tait SWG, Tang D, Tavernarakis N, Thorburn A, Tsujimoto Y, Turk B, Vanden Berghe T, Vandenabeele P, Vander Heiden MG, Villunger A, Virgin HW, Vousden KH, Vucic D, Wagner EF, Walczak H, Wallach D, Wang Y, Wells JA, Wood W, Yuan J, Zakeri Z, Zhivotovsky B, Zitvogel L, Melino G and Kroemer G. Molecular mechanisms of cell death: recommendations of the Nomenclature Committee on Cell Death 2018. Cell Death Differ 2018; 25: 486-541.

[39] Liu S, Yang T, Ming TW, Gaun TKW, Zhou T, Wang S and Ye B. Isosteroid alkaloids from Fritillaria cirrhosa bulbus as inhibitors of cigarette smoke-induced oxidative stress. Fitoterapia 2020; 140: 104434.

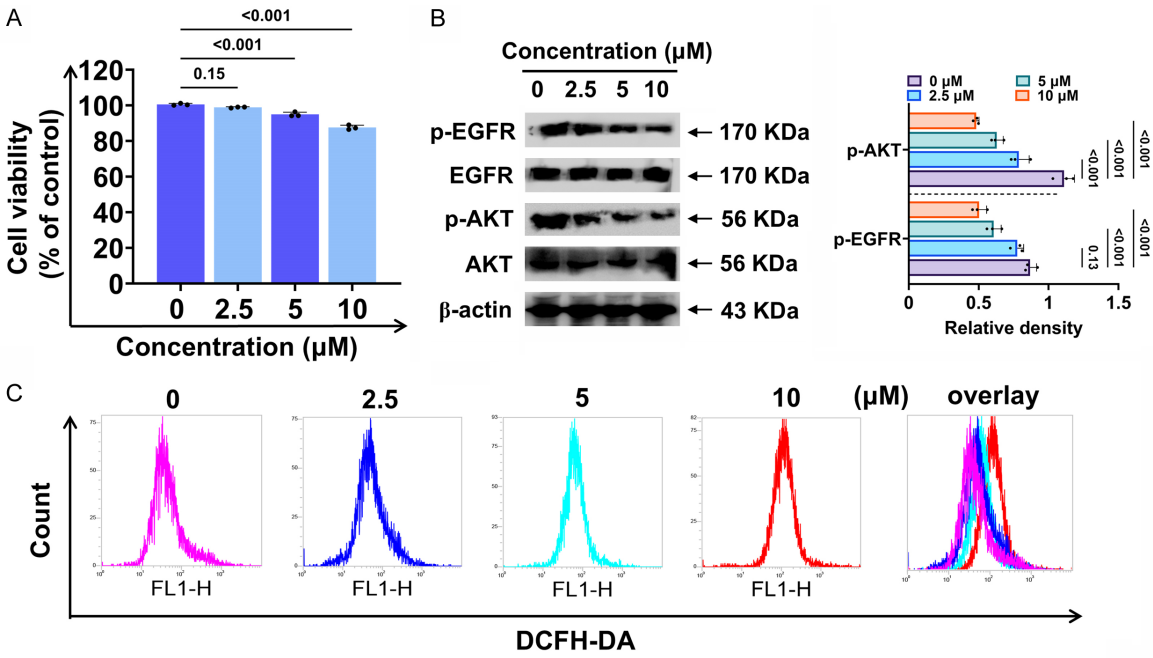
[40] Li F, Dong X, Lin P and Jiang J. Regulation of Akt/FoxO3a/Skp2 axis is critically involved in berberine-induced cell cycle arrest in hepatocellular carcinoma cells. Int J Mol Sci 2018; 19: 327.

Supplementary Table 1. Molecular docking parameters of HUP with candidate target proteins

Target	PDB ID	Grid center (x, y, z), Å	Grid points (x×y×z)	Spacing (Å)	GA runs
AKT1	1H10	18.057, 14.703, 10.033	126×112×126	0.425	10
Bcl-2	1G5M	1.344, -4.153, 2.012	112×126×92	0.4417	10
EGFR	1M14	8.207, 9.731, 40.378	126×102×126	0.8139	10
HSP90AA1	1BYQ	34.109, -48.789, 53.742	96×112×120	1.000	10
SRC	1A07	33.935, 10.168, 30.427	126×68×104	0.6639	10
TNF	1A8M	20.205, 44.849, 39.736	70×110×96	0.9194	10

Supplementary Table 2. Detailed information of primary antibodies used in Western blot analysis

Target Protein	Manufacturer	Catalog Number	Working Dilution
β-actin	Santa Cruz Biotechnology	sc-47778	1:1000
Bad	Santa Cruz Biotechnology	sc-8044	1:1000
Bcl-2	Santa Cruz Biotechnology	sc-7382	1:1000
Bax	Santa Cruz Biotechnology	sc-493	1:1000
Cyto-C	Santa Cruz Biotechnology	sc-13156	1:1000
pro-caspase-3	Santa Cruz Biotechnology	sc-7148	1:1000
cle-caspase-3	Santa Cruz Biotechnology	sc-271028	1:1000
pro-PARP	Santa Cruz Biotechnology	sc-8007	1:1000
cle-PARP	Beyotime	AF-1567	1:1000
p-EGFR	Beyotime	AF-1429	1:1000
EGFR	Beyotime	AF-1330	1:1000
p-PI3K	Beyotime	AF-5905	1:1000
PI3K	Beyotime	AF-7742	1:1000
p-AKT	Santa Cruz Biotechnology	sc-7985-R	1:1000
AKT	Santa Cruz Biotechnology	sc-8312	1:1000
NF-κB	Santa Cruz Biotechnology	sc-8008	1:1000
I-κB	Santa Cruz Biotechnology	sc-1643	1:1000
Nrf2	Beyotime	AF-7623	1:1000
HO-1	Beyotime	AF-1333	1:1000
SOD	Beyotime	AF-8028	1:1000
CAT	Beyotime	AF-0084	1:1000
Gpx1	Beyotime	AF-7017	1:1000
CDK2	Santa Cruz Biotechnology	sc-163	1:1000
CDK4	Santa Cruz Biotechnology	sc-260	1:1000
CDK6	Santa Cruz Biotechnology	sc-177	1:1000
Cyclin D	Santa Cruz Biotechnology	sc-753	1:1000
Cyclin E	Santa Cruz Biotechnology	sc-182	1:1000
p21	Santa Cruz Biotechnology	sc-397	1:1000
p27	Santa Cruz Biotechnology	sc-528	1:1000
p-GSK3β	Santa Cruz Biotechnology	sc-373800	1:1000
GSK3β	Santa Cruz Biotechnology	sc-377213	1:1000
β-catenin	Santa Cruz Biotechnology	sc-7963	1:1000
SNAI1	Santa Cruz Biotechnology	sc-271977	1:1000
E-cadherin	Santa Cruz Biotechnology	sc-8426	1:1000
N-cadherin	Santa Cruz Biotechnology	sc-59987	1:1000



Supplementary Figure 1. Early concentration-related effects of HUP on cell viability and EGFR/ROS/AKT signaling in HepG2 cells. HepG2 cells were treated with HUP at 0, 2.5, 5, and 10 μM for 6 h. A. Cell viability was assessed using the CCK-8 assay. B. Representative western blot images of p-EGFR, EGFR, p-AKT, AKT, and β-actin, with quantitative analyses of p-EGFR/EGFR and p-AKT/AKT. C. Representative DCFH-DA flow cytometric histograms and overlay plots showing intracellular ROS levels. Data are presented as mean ± SD from three independent experiments. Comparisons with the untreated control were performed using Dunnett's multiple comparisons test.